First-principles calculation for design of superconductor

Akitaka Nakanishi

MARCH 2011

First-principles calculation for design of superconductor

A dissertation submitted to

THE GRADUATE SCHOOL OF ENGINEERING SCIENCE

OSAKA UNIVERSITY

inpartial fulfillment of the requirements for the degree of

DOCTOR OF PHILOSOPHY IN SCIENCE

BY

Akitaka Nakanishi

MARCH 2011

Abstract

We performed three types first-principles calculations and compared the results with experimental facts. in order to get policies for designing the phonon-mediated superconductor with high critical temperature.

First, we simulated the critical temperature of already-known superconductors, $CaSi_2$ and phosphorus, under higher pressure. The $CaSi_2$ transformed from the trigonal structure to the AlB_2 structure at 17 GPa. After the transition, the critical temperature increases because atomic oscillation direction of E_{2g} phonon mode is parallel to the covalent bonding direction of silicons. As for the phosphorus, the critical temperature of modulated structure is lower than that of simple cubic and simple hexagonal structures, because the density of states at Fermi level is reduced by the modulation.

Second, we simulated the critical temperature of NaFeAs, NaCoAs and NaNiAs. NaFeAs has been found as FeAs superconductor. NaCoAs and NaNiAs are virtual materials in which Fe atoms of NaFeAs are substituted by Co or Ni. We simulated the critical temperature of three materials and determined NaFeAs is not phonon-mediated superconductor because the calculated $T_c = 0.034\,\mathrm{K}$ is lower than experimental data $T_c = 12\,\mathrm{K}$. The NaNiAs has the largest electron-phonon interaction and the highest T_c, because some phonon modes expand and contract the covalent bondings of Ni and As. As for the NaFeAs and the NaCoAs, these modes do not have strong interaction because they have non-covalent bonding bands at Fermi level.

Third, we simulated the property of $CuAlO_2$ under higher pressure or with doped. The superconductivity of $CuAlO_2$ has not been observed, while this is already known as semiconductor. At $P_c = 60$ GPa, the $CuAlO_2$ transforms from the delafossite structure to the leaning delafossite structure. The energy gap rises and falls in both structure phases. The metalization is not observed

under 100 GPa. The Self-interaction correction remove the discrepancy of the energy gap between experimental data and the results calculated within local density approximation. The $0.2 \sim 0.3$ hole-doped $CuAlO_2$ has relatively high $T_c \simeq 40$ K because the atomic oscillation direction of A_1L_1 phonon mode is parallel to th direction of O-Cu-O covalent bondings. Doped over 0.6 hole, the critical temperature decreases to about 10 K because the electrons strongly interacting with A_1L_1 mode phonon are removed.

From these results, we got two policies for designing the high T_c phonon-mediated superconductor: 1)The direction of covalent bonding is parallel to that the atomic oscillation direction of some phonon mode, and 2)The covalent bonding bands locate at Fermi level.

Contents

Chapter 1

Introduction

Designing new materials is a big issue among the theoretical study. It requires the reliable theory which is able to reproduce the experimental facts. As for phonon-mediated superconductors, the strong coupling theory enables us to quantitatively calculate the superconducting critical temperature. This explain the superconductivity of pure substances, A15 structure materials, MgB_2 and so on. In this thesis, we study the several materials by using the strong coupling theory and would like to understand what determines the critical temperature T_c of the phonon-mediated superconductors.

First, the targets are $CaSi_2$ and phosphorus. These are already-known pressure-induced superconductor. We predicted the crystal structure and the critical temperature in pressure range where these materials have not been researched in theoretical study.

Second, the targets are NaFeAs, NaCoAs and NaNiAs. NaFeAs has been found as FeAs superconductor while NaCoAs and NaNiAs have not been found as the real materials. We simulated the critical temperature of three materials and discussed the difference in their electronic structures and superconducting properties.

Third, the target is $CuAlO_2$. This is already known as semiconductor. It has not been observed that $CuAlO_2$ shows the superconductivity. We calculated the property of pressured and doped $CuAlO_2$ and discussed whether it can be high T_c superconductor.

Finally, we concluded the policy for designing the high T_c phonon-mediated superconductor.

Chapter 2

$CaSi_2$

2.1 Introduction

At the ambient pressure. calcium di-silicide, $CaSi_2$, has a rhombohedral crystal structure. In this structure, $CaSi_2$ is a semimetal and not a superconductor down to 0.03 K.[1] At about 10 GPa, the rhombohedral $CaSi_2$ transforms into a trigonal structure.[2] The trigonal structure has corrugated honeycomb Si networks. Between two Si networks, Ca atoms are intercalated, forming a triangular lattice plane. Each Ca atom locates just above the center of one corrugated hexagon of Si atoms. In this structure, $CaSi_2$ is a superconductor with the critical temperature $T_c \simeq 3$ K.[3] At about 15 GPa, structural phase transformation takes place and the corrugated Si networks become "nearly" flat. If the Si networks is "perfectly" flat, the crystal structure is AlB_2 structure. Because the Si networks remain corrugated, this structure of $CaSi_2$ is called the AlB_2-like structure.[2] In the AlB_2-like structure, T_c increases up to around 14 K. This temperature is the highest among Si-based compounds. Here, we note that before these experimental findings, the structural transition from the trigonal structure to the AlB_2 structure has been predicted

theoretically.[4]

After MgB_2 have been found to be a high-temperature superconductor,[5] the superconductivity in the AlB_2 structure attracted much attention. As for $CaSi_2$, theoretical studies were done in low-pressure phases.[6, 7] Satta *et al.* considered possibility of the AlB_2 structure under high pressure and however, they could not find this structure with fixed cell parameters.[8] The electron-phonon interaction and the superconducting critical temperature were rarely estimated theoretically.[9] Thus, $CaSi_2$ has not been studied so often in the literature compared with MgB_2.

The purpose of this study is to clarify stable structures and superconductivity of $CaSi_2$ under high pressure. Using first-principles calculation, we optimized the crystal structures and studied electronic band structures, phonon dispersion and superconducting critical temperatures. Our results show that $CaSi_2$ transforms to the AlB_2 structure and that T_c will increase after the transition.

2.2 Methods

First-principles calculations were performed within the density functional theory[10, 11] with a plane-wave pseudopotential method, as implemented in the Quantum-ESPRESSO code.[12] We used the Perdew-Wang generalized gradient approximation exchange-correlation functional[13] and ultrasoft pseudopotentials.[14] For the pseudopotentials, Ca 3d electrons were also included in valence electrons. Atomic positions and cell parameters were optimized by the constant-pressure variable-cell relaxation using the Parrinello-Rahman method[15] without any symmetry requirements.

We used a $12 \times 12 \times 12$ **k**-point grid (electron) and a $4 \times 4 \times 4$ **q**-point

grid (phonon) in the Monkhorst-Pack grid.[16] The energy cut-off for the wave functions is 16 Ry and that for the charge density is 64 Ry. Though these values may be comparatively small, the accuracy is enough. This is confirmed by the calculations with larger energy cut-offs of 40 Ry and 160 Ry, resulting in "almost the same" optimized structure.

We estimated superconducting critical temperature T_c using the strong coupling theory.[17] The electron-phonon matrix is calculated by the density functional perturbation theory.[18]

The space-group of the trigonal lattices of $CaSi_2$ is $P\bar{3}m1$ (No.164) and that of AlB_2 structure is $P6/mmm$ (No.191). The Wyckoff position of the calcium atom at the $1a$ site of $P\bar{3}m1$ is given by $(0, 0, 0)$, while those of two silicon atoms at the $2d$ sites are $(1/3, 2/3, z)$ and $(2/3, 1/3, \bar{z})$ with the internal parameter z. The trigonal structure with $z = 0.5$ is identical to the AlB_2 structure.

In this study, we consider the pressure range of $P = 10 \sim 20$ GPa because superconductivity does not appear below 10 GPa.

2.3 Results and Discussion

2.3.1 Structural optimization under high pressure

Fig. 2.1 shows optimized lattice parameters. From 10 to 15 GPa, the calculated lattice parameters agree with experimental data.[2] The relative errors are less than 2%. Above 17 GPa, however, the calculated lattice parameters disagree with experimental data. Especially, calculated internal parameter z is 0.5, while in the experiment it does not reach 0.5. Our result shows that $CaSi_2$ has the AlB_2 structure above 17 GPa where experiment shows that $CaSi_2$ has AlB_2-like structure.

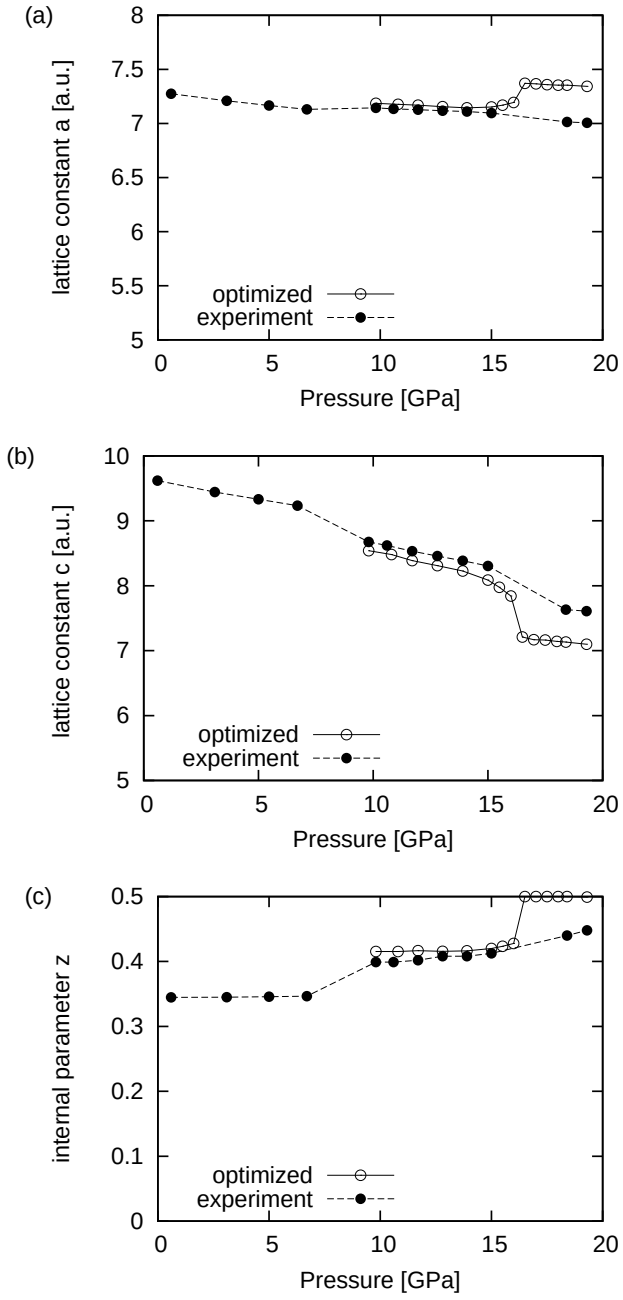

Figure 2.1: Pressure dependence of lattice parameters: (a) lattice constant a, (b) lattice constant c, and (c) internal parameter z. The parameters are obtained by the structural optimization at each pressure, and they are represented by open circles. The experimental data[2] is represented by closed circles.

This discrepancy is not attributed to the pseudopotential method used here. We checked results of all electron methods: the full potential linear muffin tin orbital method and the full potential linearized augmented-plane wave method. The former is implemented in the packaged code developed by S. Y. Savrasov and D. Y. Savrasov.[19] The latter is implemented in the WIEN2k code.[20] By using both methods, we optimized the structure with constant cell volume. The results indicate that the AlB_2 structure is more stable than the trigonal structure under high pressure. Here, we note that the pressures obtained by the first-principles calculation could have an error. For example, the pressures of calcium calculated by the same method as this study are much lower than experimental data.[21]

To test stability of the AlB_2 structure, we checked the phonon frequency in the whole Brillouin zone. Only real frequencies appear all over the Brillouin zone as shown later (Fig. 2.6). We expect that the AlB_2 structure will be observed under higher pressure in the experiment.

Fig. 2.2 shows enthalpy of some atomic structures. Each structure is given by optimizing c/a with fixing z. This figure indicates that $CaSi_2$ abruptly transforms from the trigonal structure ($z = 0.42$) to the AlB_2 structure ($z = 0.5$). In our calculation, $CaSi_2$ does not transform from the trigonal structure to the AlB_2-like structure ($z = 0.44$).

2.3.2 Electronic band structure

Fig. 2.3(a) and (b) show the band structures of $CaSi_2$ in trigonal and ALB_2 structures. An electronic band structure of $CaSi_2$ in the AlB_2 structure was studied in earlier works.[4, 8] There are some differences between the present result and the earlier one. This is due to whether the lattice parameters are optimized (this study) or not (earlier one).

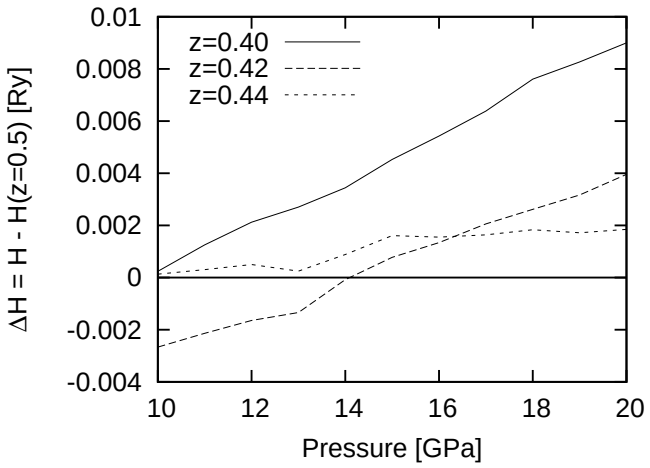

Figure 2.2: Enthalpy of $CaSi_2$ under high pressure. Lattice parameters of each structures are determined with a fixed z. The enthalpy of AlB_2 structure ($z = 0.5$) is set to be 0 Ry.

Fig. 2.3 (a) shows the band structure of the trigonal structure. Bands crossing the Fermi level show Si p_z, Ca d and Si p_z-Ca d hybridized characters. Since the Si planes are corrugated, p_z bands of Si should rather be called "$\pi(\pi^*)$-like" band.

Fig. 2.3 (b) shows the band structure of the AlB_2 structure. First, we can observe d-character in some σ^* bands near the Fermi level. We should note that for a Ca compound under high pressure Ca d-orbitals often appear at the Fermi level. For example, appearance of the d character was pointed out theoretically for CaSi in the CuAu structure and $CaSi_3$ in the $CuAu_3$ structure.[6] Second, the π^* band lies also near the Fermi level. Comparing with Fig. 2.3 (a), it looks that the electrons are moved from the σ^* bands to π^* bands. Third, the doubly degenerated p-d hybridized bands at the A point form the Fermi pockets. Along the A-L symmetry line, one of those bands becomes almost dispersion-less. The dispersion-less band enhance the

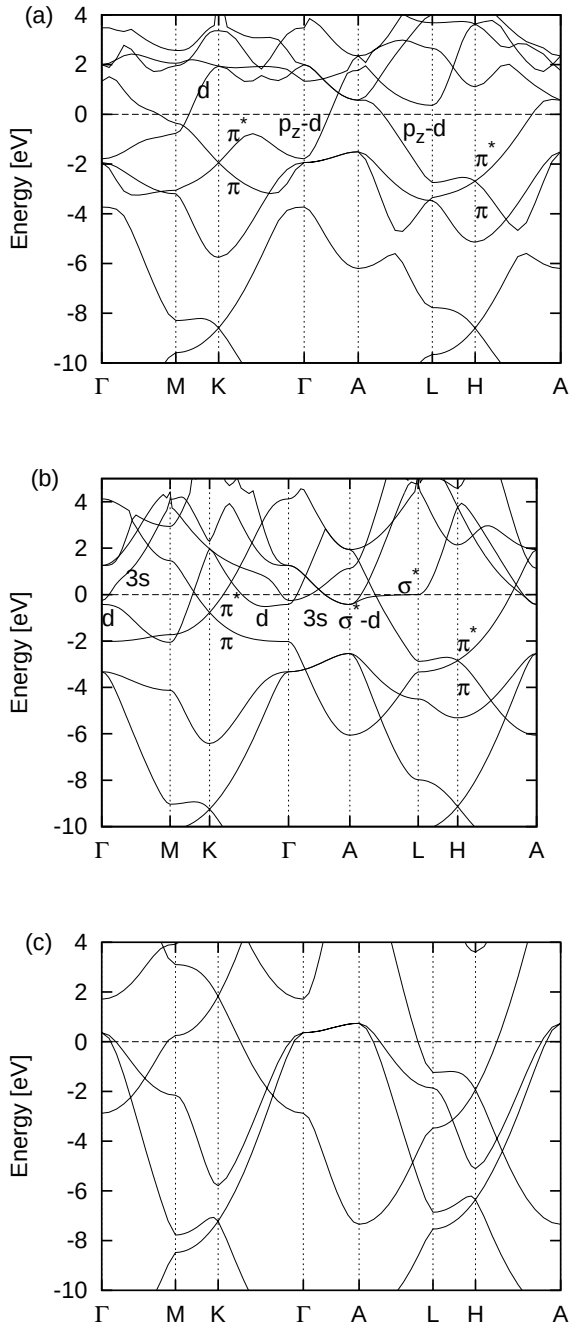

Figure 2.3: Electronic band structure of the optimized structures of $CaSi_2$ in (a) the trigonal structure and (b) AlB_2 structure. (c) The electronic band structure of MgB_2.

density of states around the Fermi level as shown below.

Fig. 2.4 shows the pressure dependence of density of states at the Fermi level. Through the structural transition, the density of states increases, because in the AlB_2 structure the s, d and σ^*-d bands go down to Fermi level and make electron pockets as shown in Fig. 2.3.

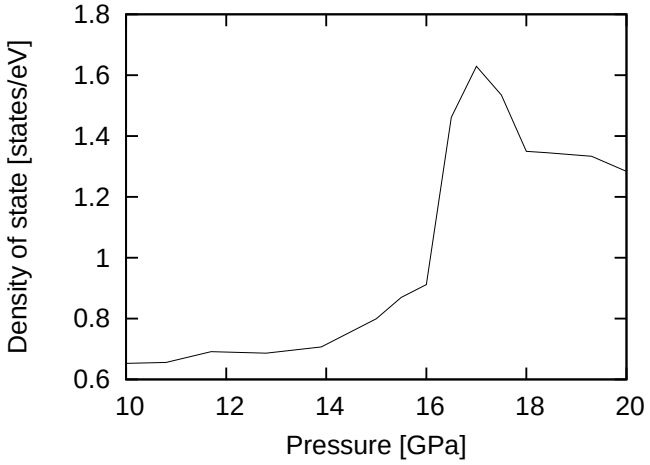

Figure 2.4: Pressure dependence of the density of states at the Fermi level. It suddenly increases when the structure transforms to the AlB_2 structure.

Here, we compare the electronic band structure of $CaSi_2$ with that of MgB_2 (Fig. 2.3 (c)). These materials in AlB_2 structures have both π- and σ-bands of sp^2-hybridized orbitals. The σ bands of MgB_2 looks to be partly hole-doped creating small two-dimensional hole pockets.[22] In $CaSi_2$, on the other hand, σ bands are fully occupied and a flat σ^* band lies along the A-L line around the Fermi level. The MgB_2 has only π- and σ-bands. The $CaSi_2$, however, has additional bands around the Fermi level: Ca $3d$ bands, Si $3s$ band, and σ^*-d hybridized bands.

2.3.3 Superconducting critical temperature

Fig. 2.5 shows superconducting critical temperature. Our results that through the structural transition, T_c suddenly increases and reaches to a value one order of magnitude larger than those in the low pressure phase. In the trigonal structure, calculation results are almost one-tenth of the experimental data,[23] which is about $3 \sim 4\,\mathrm{K}$. This discrepancy may be due to utilization of an isotropic approximation in the Eliashberg theory (See Appendix).

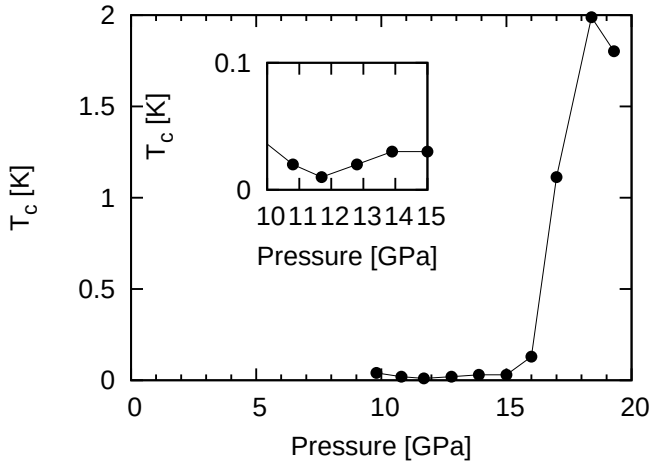

Figure 2.5: Pressure dependence of T_c. From 10 to 17 GPa, $CaSi_2$ has the trigonal structure with the corrugated silicon network and above 17 GPa, it transforms to the AlB_2 structure with the perfectly flat silicon network.

Let us discuss why T_c increases after the structural transition. According to the Allen-Dynes modified McMillan's formula,[24, 25] T_c is given by three factors: the electron-phonon interaction λ, the logarithmic averaged phonon frequency $\omega_{\log}$, and the screened Coulomb interaction μ^*, in the following form.

$$T_c = \frac{\omega_{\log}}{1.2} \exp\left(-\frac{1.04(1+\lambda)}{\lambda - \mu^*(1+0.62\lambda)}\right). \tag{2.1}$$

Here λ and $\omega_{\log}$ are obtained by the density functional perturbation theory. As for μ^*, we assume the value $\mu^* \sim 0.1$. This value holds for weak correlated systems. In this study, the critical temperature is determined by λ and $\omega_{\log}$. The table 2.1 shows λ and $\omega_{\log}$. While $\omega_{\log}$ decreases about 10%, λ increases about 50%. Therefore, the increase of λ leads to the increase of T_c.

structure	λ	$\omega_{\log}[K]$
trigonal(10GPa)	0.27	300
AlB_2 (20GPa)	0.41	280

Table 2.1: Electron-phonon interaction λ and logarithmic averaged phonon frequencies $\omega_{\log}$.

Here, we analyze the electron-phonon interaction. The parameter λ is given explicitly as follows.

$$\lambda \equiv 2\int_0^\infty d\omega \frac{\alpha^2 F(\omega)}{\omega}, \tag{2.2}$$

using the Eliashberg function $\alpha^2 F(\omega)$,

$$\alpha^2 F(\omega) = \frac{N(0)\sum_{\mathbf{k}\nu\mathbf{q}} |M^{\nu\mathbf{q}}_{\mathbf{k},\mathbf{k}+\mathbf{q}}|^2 \delta(\omega - \omega_{\nu\mathbf{q}})\delta(\varepsilon_{\mathbf{k}})\delta(\varepsilon_{\mathbf{k}+\mathbf{q}})}{\sum_{\mathbf{kq}} \delta(\varepsilon_{\mathbf{k}})\delta(\varepsilon_{\mathbf{k}+\mathbf{q}})}. \tag{2.3}$$

Here, $N(0)$ is electronic density of states with a single spin component at the Fermi level, which is set to be 0. $\omega_{\nu\mathbf{q}}$ and $\varepsilon_{\mathbf{k}}$ are phonon and electron energies. $M^{\nu\mathbf{q}}_{\mathbf{k},\mathbf{k}+\mathbf{q}}$ is the electron-phonon matrix elements. For the mode analysis, we introduce partial electron-phonon interaction $\lambda_{\nu\mathbf{q}}$ so that $\lambda = \sum_{\nu\mathbf{q}} \lambda_{\nu\mathbf{q}}$. It is defined by the following form.

$$\lambda_{\nu\mathbf{q}} = \frac{2N(0)\sum_{\mathbf{k}} |M^{\nu\mathbf{q}}_{\mathbf{k},\mathbf{k}+\mathbf{q}}|^2 \delta(\varepsilon_{\mathbf{k}})\delta(\varepsilon_{\mathbf{k}+\mathbf{q}})}{\omega_{\nu\mathbf{q}} \sum_{\mathbf{kq}'} \delta(\varepsilon_{\mathbf{k}})\delta(\varepsilon_{\mathbf{k}+\mathbf{q}'})}. \tag{2.4}$$

Using $\lambda_{\nu\mathbf{q}}$ we find the most influential phonon mode for the superconductivity and T_c. In Fig. 2.6, the magnitude of $\lambda_{\nu\mathbf{q}}$ is represented by radius of circle on each phonon dispersion. This figure indicates that, in the AlB_2 structure, the highest mode at the Γ point is effective. This mode is the E_{2g} mode. In this mode, the neighboring silicon atoms oscillate in the anti-phase within a Si plane. This feature is the same as that observed in MgB_2.[26] The E_{2g} mode is a key of the high-temperature superconductivity of MgB_2.

In addition, we see another effective mode in the AlB_2 structure. This mode is the B_{1g} mode. In this mode, the neighboring silicon atoms oscillate in the anti-phase perpendicularly to a Si plane. This displacement makes the Si plane corrugated. Frequencies of B_{1g} are softened around the Γ point. Due to the softening, $\lambda_{\nu\mathbf{q}}$ has a large value. However, the softening may reduce $\omega_{\log}$ given by

$$\omega_{\log} = \exp\left(\frac{2}{\lambda}\int_0^\infty d\omega \frac{\alpha^2 F(\omega)}{\omega}\log\omega\right), \tag{2.5}$$

and does not necessarily work to increase the critical temperature as exemplified in iodine.[27] In the case of $CaSi_2$, the AlB_2 structure has higher frequency optical branches than the trigonal structure. As a result, $\omega_{\log}$ and T_c are not decreased by the phonon softening. This means that both B_{1g} and E_{2g} phonon modes contribute to enhancement of electron-phonon interaction and superconducting critical temperature.

2.4 Summary

In this chapter, we optimized the crystal structure of $CaSi_2$ under high pressure by using first-principles calculations. Our results show that AlB_2 structure is stable above 17 GPa. The density of states at the Fermi level in the AlB_2 structure is higher than that in the trigonal structure. After the

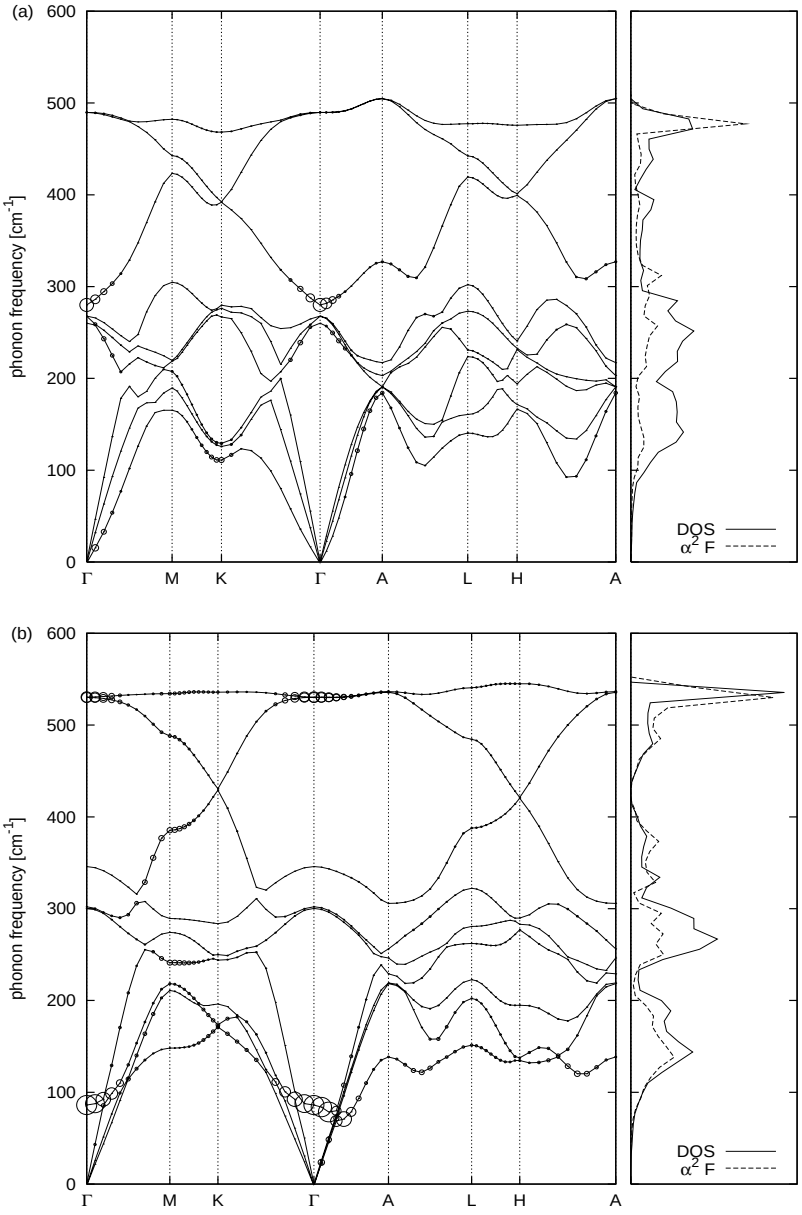

Figure 2.6: Phonon dispersions, density of states and Eliashberg functions of $CaSi_2$ in (a) an optimized trigonal structure (10 GPa) and (b) an optimized AlB_2 structure (20 GPa). The radius of circle displays the magnitude of partial electron-phonon interaction $\lambda_{\nu\mathbf{q}}$. The definition is explained in the text.

transition, E_{2g} and B_{1g} phonon modes have a strong interaction with electrons because corrugated Si network becomes flat. High frequencies of the E_{2g} mode phonon prevent decrease of $\omega_{\log}$ and T_c by B_{1g} phonon softening. These findings suggest that the AlB_2 structure has higher T_c than the trigonal structure.

Chapter 3

Phosphorus

3.1 Introduction

Phosphorus has a A17 structure (phase I) at the ambient pressure. The A17 structure transforms to the A7 structure (phase Ⅱ) at 4.5 GPa. The A7 phosphorus transtorms to simple cubic structure (phase Ⅲ) at 10GPa. In this structure, phosphorus shows the superconductivity. The critical temperature T_c has a maximum of 9.5 K at 32 GPa. and decreases to 4.3 K at 100 GPa.[28] Akahama *et al.* reported that through an intermadiate structure (phase Ⅳ), a simple cubic phosphorus transforms to a simple hexagonal structure (phase V) at 137 GPa.[29] Under higher pressures, the body centered cubic structure (phase VI) has been theoretically predicted[30] and later experimentally observed at 262 GPa.[31] At this time, the crystal structure of Ⅳ phase, however, was not identified experimentally. Ordinary the Rietveld analysis based on a knowledge of the monoclinic symmetry was not successfull, presumably owing to he complexity of the lattice.

To determine the structure of Ⅳ phase, many theoretical studies have been reported. Ahuja considered a structure of space group *Imma*.[32] Ehelrs

and Christensen investigated relative stability of the Ba-IV structure which is an incommensurate composite structure against sc and sh.[33] The calculated x-ray diffraction patterns of these structures, however, disagree with the experimental pattern of IV phase. In 2005 Ishikawa *et al.* explored the structure of IV phase by the first-principle metadynamics simulation and predicted another candidate structure which has the incommensurately modulated structure.[34] The calculated diffraction pattern of the modulated structure matches the experimental pattern.

Recently Fujihisa *et al.* has experimentally determined the structure of IV phase by a Rietveld analysis.[35] The structure if the incommensurately modulated structure along c axis with a monoclinic distortion $\gamma = 97.8°$. They also reported that the modulation wave vector along c axis is 0.268 at 113 GPa and it decreases to 0.266 at 137 GPa. This structure is almost identical to Ishikawa's theoretically predicted structure.

As shown above, theoretical and experimental studies showed that I V phase structure is modulated structure. Superconducting properties in this structure, however, has not been studied well theoretically and experimentally. In this study, we have simulated superconducting critical temperature in the modulated structure by using first-principles calculation.

3.2 Methods

The crystal structure of IV phase is incommensurate modulated structure. It belongs to the superspace group $Cmmm(00\gamma)s00$ with $\gamma = 0.2673(1/\gamma = 3.741)$ at 125 GPa.[35] It needs a large supercell to deal with the incommensurate structure exactly by using first-principles calculation. We approximated the incommensurate structure by commensurate one with $1/\gamma = 4$. Fig. 3.1

shows the approximated structure. Atomic positions of the approximated structure in crystal coordinate are following; $(0,0,0),(0,0,1/2),(y,y,1/4)$, and $(-y,-y,3/4)$.

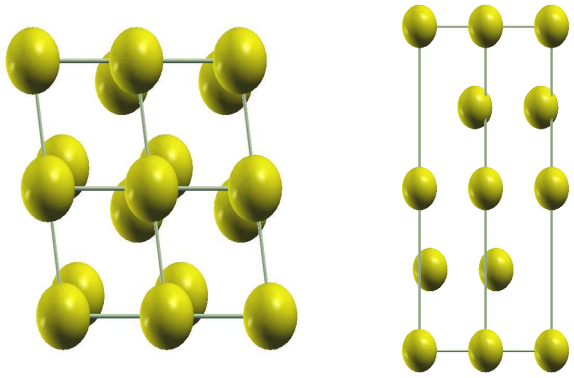

(a) (b)

Figure 3.1: Approximated crystal structure of phosphorus Ⅳ phase($1/\gamma \simeq 4$): (a)the xy-plane top view, (b)the yz-plane side view.

First-principles calculations were performed within the density functional theory[10, 11] with a plane-wave pseudopotential method, as implemented in the Quantum-ESPRESSO code.[12] We employed the Perdew-Burke-Ernzerhof generalized gradient approximation exchange-correlation functional[36] and ultra-soft pseudo-potentials.[14]

We optimized crystal cells of simple cubic phase($10 \sim 100$GPa), Ⅳ phase ($110 \sim 130$GPa), and simple hexagonal phase ($140 \sim 300$GPa) and calculated superconducting critical temperatures in these phases. Atomic positions and cell parameters were optimized by the constant-pressure variable-cell relaxation using the Parrinello-Rahman method[15] without any symmetry requirements. We estimated the superconducting critical temperature $T_{\rm c}$ using the strong coupling theory.[17, 25] The electron-phonon matrix was calculated by the density functional perturbation theory.[18]

In electronic calculation, we used $32 \times 32 \times 32$ (sc, sh) and $32 \times 32 \times 8$ (IV) **k**-point grid in the Monkhorst-Pack grid.[16] In phonon calculation, we used $8 \times 8 \times 8$ (sc, sh) and $8 \times 8 \times 2$ (IV) **q**-point grid in the same grid. Energy cut-off for wave function is 40 Ry and that for charge density is 320 Ry. These **k**-point meshes and cut-off energies are fine enough to achieve convergence within 0.1mRy/atom in the total energy.

3.3 Results and Discussion

3.3.1 Structural optimizations

Calculated lattice parameters are consistent with results simulated by Ishikawa *et al.*.[34] We observe that only real frequencies appear all over the Brillouin zone. This result indicates that approximated structure is sufficient to discuss superconducting properties.

3.3.2 Superconducting critical temperature

Fig. 3.2 shows calculation results of T_c, λ and ω_{log}. The calculated critical temperature above 30 GPa is consistent with observed values in experiment.[28] Below 30 GPa, however, calculated T_c is decreasing, while experimentally observed one is increasing. This discrepancy may mean that A7 structure remains until 30 GPa. The IV phase has lower critical temperature than the other phases.

Let us examine the origin of the low T_c. According to the Allen-Dynes modified McMillan's formula,[24, 25] T_c is given by three factors: the electron-phonon interaction λ, the logarithmic averaged phonon frequency ω_{log}, and

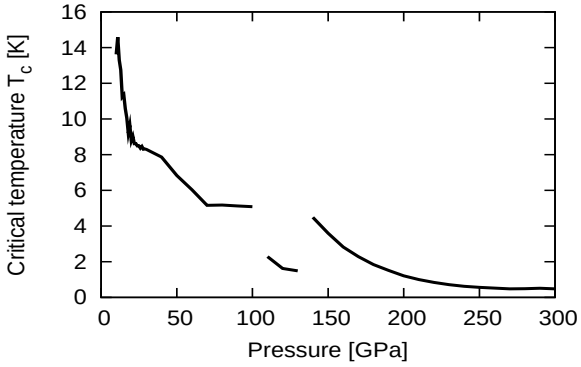

(a) Superconducting critical temperature T_c

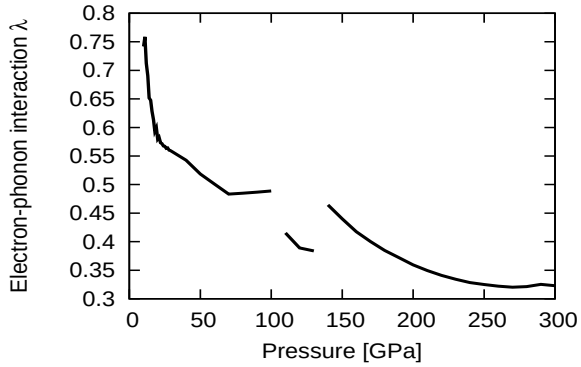

(b) Electron-phonon interaction λ

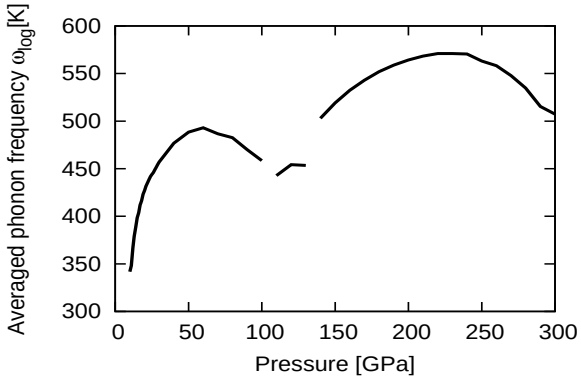

(c) Logarithmic averaged phonon frequency $\omega_{\log}$

Figure 3.2: Calculated superconducting parameters

the screened Coulomb interaction μ^*, in the following form.

$$T_c = \frac{\omega_{\log}}{1.2} \exp\left(-\frac{1.04(1+\lambda)}{\lambda - \mu^*(1+0.62\lambda)}\right). \tag{3.1}$$

Here λ and $\omega_{\log}$ are obtained by the first-principle calculations using the density functional perturbation theory. As for μ^*, we assume the value $\mu^* = 0.1$. This value holds for simple metals. In this study, the critical temperature is determined by λ and $\omega_{\log}$. Comparing pressure dependence of these, we found that the pressure dependence of the electron-phonon interaction determines that of superconducting critical temperature.

The electron-phonon interaction is strongly affected by density of states (DOS) at Fermi level. Fig. 3.3 shows calculated electronic DOS at Fermi level. The modulated structure has lower DOS than sc and sh. The small DOS is related to the modulation. The detail has already been discussed in Ishikawa's doctoral thesis[37] and Marqués's study.[38] We concluded that the small DOS decreases the electron-phonon interaction and that the small λ decreases the superconducting critical temperature.

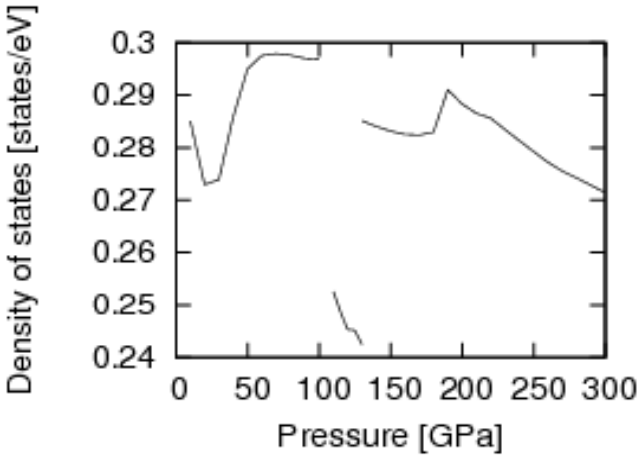

Figure 3.3: Calculated electronic density of states at Fermi level.

In each structure, the electron-phonon interaction and critical temper-

ature monotonically decrease, while the logarithmic averaged phonon frequency rises and falls. The electron-phonon interaction and the logarithmic averaged phonon frequency are defined as followings.

$$\lambda \equiv 2\int_0^\infty d\omega \frac{\alpha^2 F(\omega)}{\omega}, \tag{3.2}$$

$$\omega_{\log} \equiv \exp\left(\frac{2}{\lambda}\int_0^\infty d\omega \frac{\alpha^2 F(\omega)}{\omega}\log\omega\right), \tag{3.3}$$

Fig. 3.4 shows the density of states of phonon. This figure indicates the hardening of phonon. The hardening decreases $\alpha^2 F(\omega)/\omega$ and increases $\log\omega$. Therefore, these two competing effects make $\omega_{\log}$ rises and falls, while the former increases λ.

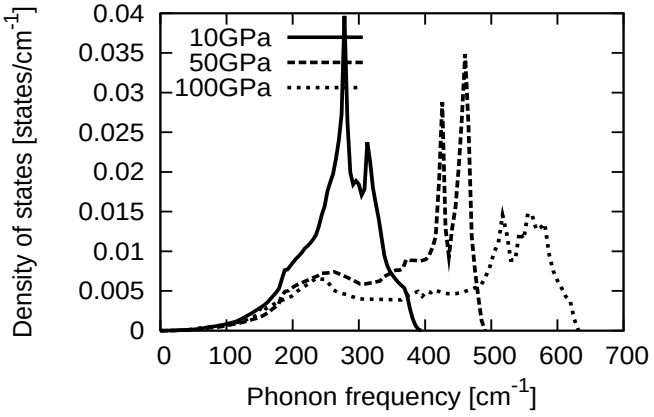

Figure 3.4: Calculated density of states of phonon.

3.4 Summary

In this chapter, we simulated the superconducting critical temperature of phosphorus under high pressure. The Ⅳ phase has lower critical temperature than the other phases. The low T_c is attributed to the small electronic DOS,

which is decreased by the modulation. As pressure increases, the electron-phonon interaction and T_c decreases due to the hardening of phonon.

Chapter 4

NaFeAs

4.1 Introduction

Recently, FeAs superconductors attract many attention, because the maximum of their superconducting critical temperatures (maximum of $T_c \simeq 55$ K) is the highest among non-cuprate superconductors. [39, 40, 41] Many experimental and theoretical studies suggest that the superconductivity of FeAs compounds are not explained only by electron-phonon interaction. But, we should note that the electron-phonon interaction may be important because the isotope effect is observed. NiAs compounds are also superconductors and are considered to be conventional phonon-mediated superconductors. According to our best knowledge, superconductivity of CoAs has not been observed.

To study the material dependence of the pnictides is main purpose of this chapter. For this purpose, we considered the electronic and phonon structure of NaFeAs and substitutions of Fe by other transition metals: Co and Ni. NaFeAs is one of pnictide superconductors and shows superconductivity without doping at the ambient pressure,[42, 43] while many FeAs compounds

show superconductivity under pressure or with doped.

4.2 Methods

In this study, targets are NaFeAs, NaCoAs and NaNiAs. We calculated the electronic band structure, the density of states, the Fermi surface, the phonon dispersion, the electron-phonon interaction, and the superconducting critical temperature of these materials as following methods.

First-principles calculations were performed within the density functional theory[10, 11] with a plane-wave pseudopotential method, as implemented in the Quantum-ESPRESSO code.[12] We used the Perdew-Burke-Ernzerhof generalized gradient approximation exchange-correlation functional[36] and ultra-soft pseudo-potentials.[14] For the pseudopotentials, 4s and 4p electrons of the transition metal atoms(Fe, Co and Ni) were also included in the valence electrons.

Atomic positions and cell parameters were optimized by the constant-pressure variable-cell relaxation using the Parrinello-Rahman method[15] without any symmetry requirements. Initial cells of optimizations are the experimental values of NaFeAs at ambient pressure.The space-group symmetry of NaFeAs is classified in $P4/nmm$ (No.129). The Wyckoff positions of Fe at $2a$ sites are given by $(3/4, 1/4, 0)$ and $(1/4, 3/4, 0)$, while those of Na (and As) at $2c$ sites are given by $(1/4, 1/4, z)$ and $(3/4, 3/4, -z)$ with internal parameter z. We estimated superconducting critical temperature T_c using the strong coupling theory.[17] The electron-phonon matrix is calculated by the density functional perturbation theory.[18] We used $16 \times 16 \times 16$ **k**-point grid (electron) and $4 \times 4 \times 2$ **q**-point grid (phonon). The energy cut-off for wave functions is 30 Ry and that for charge density is 240 Ry.

4.3 Results and Discussion

4.3.1 Structural optimizations

Table 4.1 shows the optimized lattice constants and internal parameters. To test the stability of virtual materials (NaCoAs and NaNiAs), we checked the phonon frequencies in the whole Brillouin zone. Only real frequencies appear all over the Brillouin zone as shown latter (Fig. 4.4). We expect the experimental feasibility for synthesis of these virtual materials: NaCoAs and NaNiAs.

	a [a.u.]	c/a	z_{Na}	z_{As}	V [a.u.^{3}]
NaFeAs	7.3795	1.7975	0.6585	0.1913	722.1248
NaCoAs	7.4257	1.7636	0.6567	0.1895	722.3534
NaNiAs	7.6197	1.6944	0.6426	0.1873	749.6000

Table 4.1: Optimized lattice parameters of NaFeAs, NaCoAs and NaNiAs.

4.3.2 Electronic band structures

Fig. 4.1 shows the band structure, the density of states and the Fermi surface of NaFeAs. There are electron pockets around the M point and hole pockets around the Γ point, which displays a semi-metallic feature. At the Fermi level, only Fe $3d$ bands appear. These bands are not covalent bonding bands. The cylindrical Fermi surfaces at the center and corner of Brillouin zone have two-dimensional nature.

Fig. 4.2 shows the band structure, the density of states and the Fermi surface of NaCoAs. Around the Γ point, the hole pockets are occupied and electron pockets appear. In addition to transition metal $3d$ bands, As $4p$

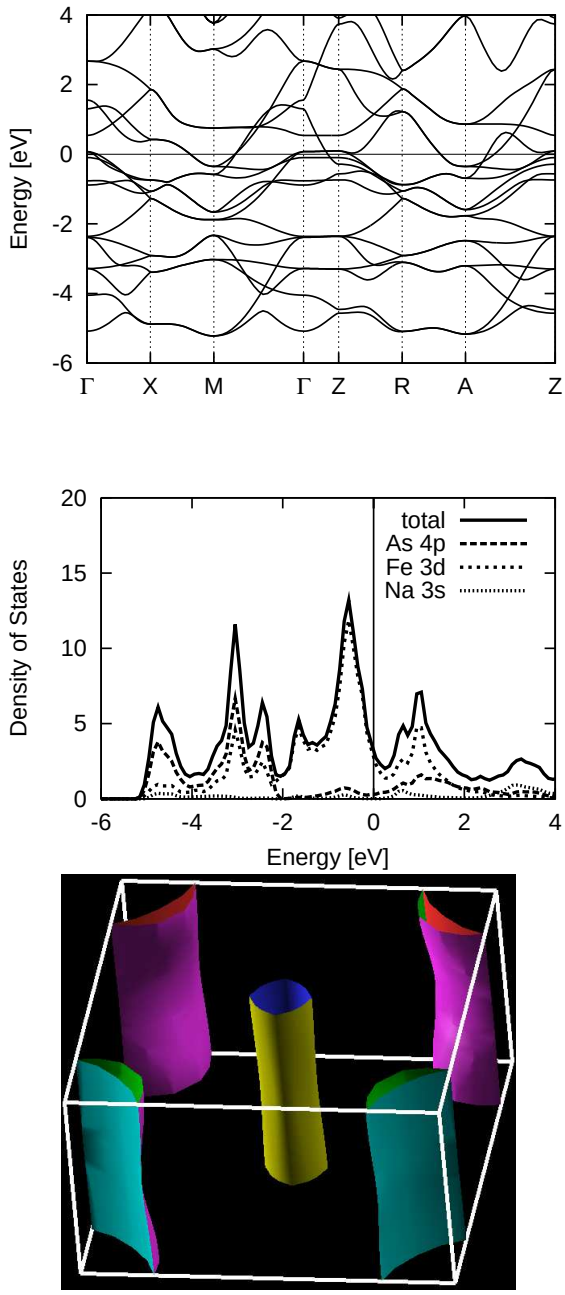

Figure 4.1: Electronic band structure (top), Density of states (center) and Fermi surface (bottom) of NaFeAs.

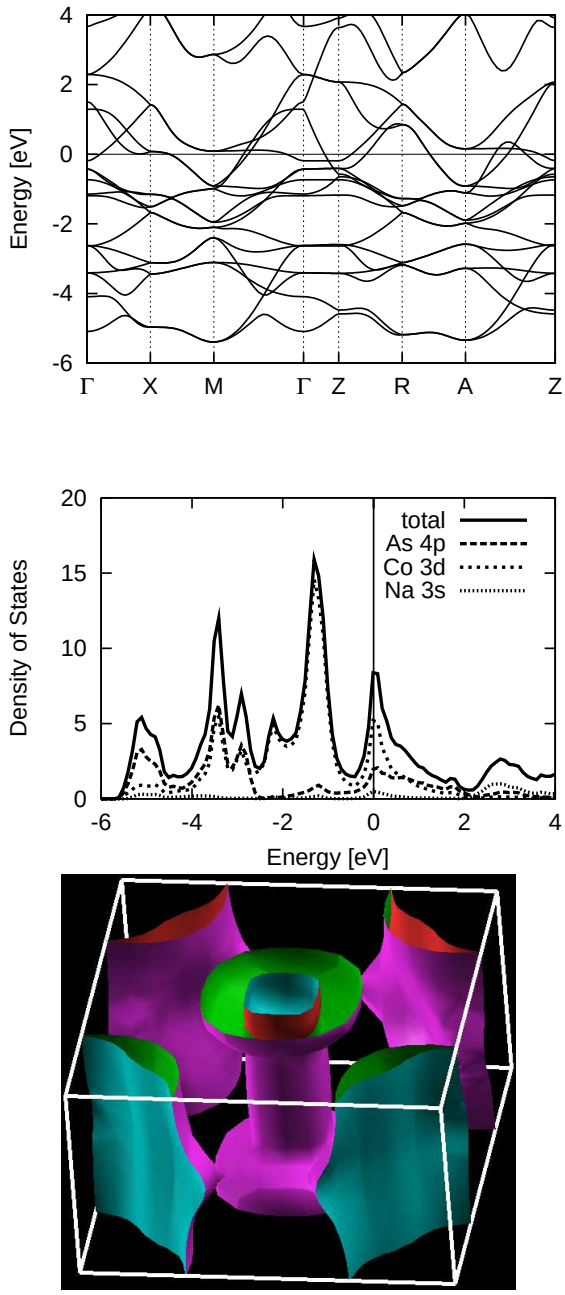

Figure 4.2: Electronic band structure (top), Density of states (center) and Fermi surface (bottom) of NaCoAs.

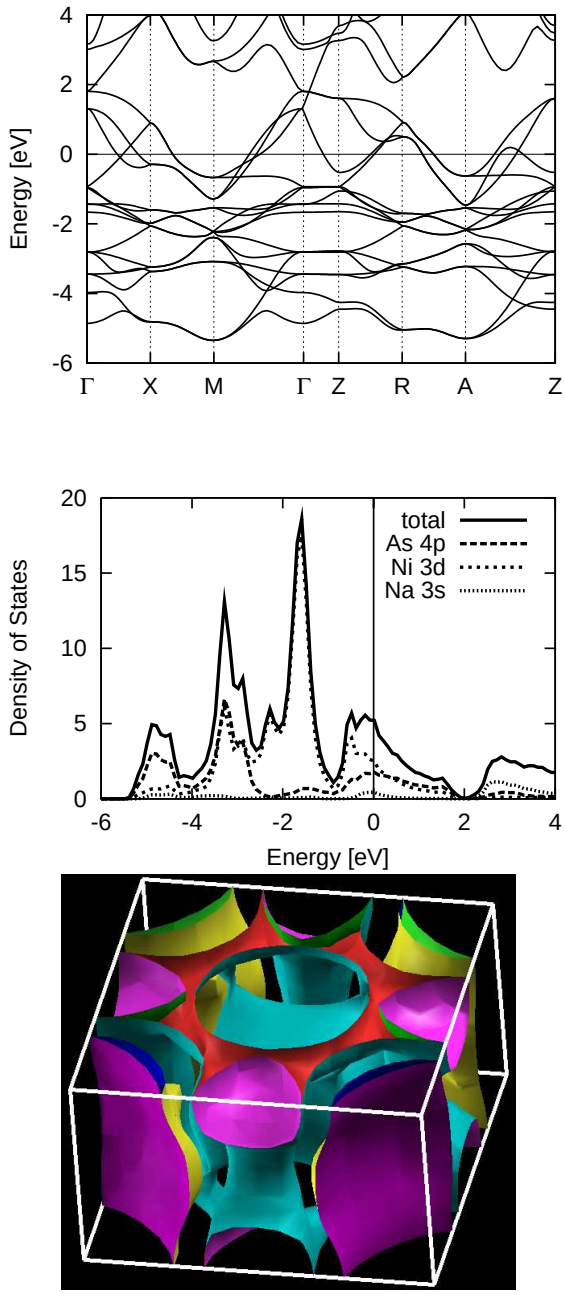

Figure 4.3: Electronic band structure (top), Density of states (center) and Fermi surface (bottom) of NaNiAs.

bands appear at the Fermi level. Two-dimensional feature of Fermi surfaces becomes less clear.

Fig. 4.3 shows the band structure, the density of states and the Fermi surface of NaNiAs. The hole pockets go down deeply and band structure is metallic. At the Fermi level, Ni 3*d*-As4*p* anti-bonding bands appear. Fermi surface is three dimensional ant the two-dimensional feature disappears.

Comparing Fig. 4.1, 4.2 and 4.3, a rigid band picture is roughly realized. Correspondence of bands is clear. The band structures of NaCoAs and NaNiAs are approximately given by heavy electron doping in the band structure of NaFeAs.

4.3.3 Superconducting critical temperature

Table 4.2 shows superconducting critical temperature of NaFeAs, NaCoAs and NaNiAs. As for NaFeAs, the calculated T_c are about 0.3% of the experimental data, which is about 12 K. [42, 43] This discrepancy suggests that NaFeAs may not be a phonon-mediated superconductor. An another group also reported the low critical temperature of NaFeAs calculated within the density functional perturbation theory.[44]

	T_c [K]	λ	$\omega_{\log}$ [K]
NaFeAs	0.034	0.275	178
NaCoAs	0.13	0.312	181
NaNiAs	3.5	0.698	103

Table 4.2: Superconducting temperature T_c, electron-phonon interaction λ and logarithmic averaged phonon frequencies $\omega_{\log}$ of NaFeAs, NaCoAs and NaNiAs. The definition is explained in the section 2.3.3.

Table 4.2 shows that T_c of NaNiAs is the highest among three compounds. Let us discuss why T_c of NaNiAs is large. According to the Allen-Dynes modified McMillan's formula,[24, 25] T_c is given by three factors: the electron-phonon interaction λ, the logarithmic averaged phonon frequency $\omega_{\log}$, and the screened Coulomb interaction μ^*, in the following form.

$$T_c = \frac{\omega_{\log}}{1.2} \exp\left(-\frac{1.04(1+\lambda)}{\lambda - \mu^*(1+0.62\lambda)}\right). \tag{4.1}$$

Here λ and $\omega_{\log}$ are obtained by the density functional perturbation theory. As for μ^*, we assume the value $\mu^* \sim 0.1$. This value holds for weak correlated systems. In this study, the critical temperature is determined by λ and $\omega_{\log}$.

Comparing NaFeAs and NaCoAs, we do not find a large difference in λ and $\omega_{\log}$. On the other hand, there are large difference between NaNiAs and the others. NaNiAs has more than twice λ and about half $\omega_{\log}$. The former increases T_c, while later decreases $\omega_{\log}$. But, λ increases T_c exponentially while $\omega_{\log}$ increases T_c linearly. Therefore, T_c of NaNiAs is the highest among three compounds.

Here, we analyze the electron-phonon interaction. For the mode analysis, we introduce partial electron-phonon interaction $\lambda_{\nu\mathbf{q}}$ so that $\lambda = \sum_{\nu\mathbf{q}} \lambda_{\nu\mathbf{q}}$, as same as section 2.3.3.

Using $\lambda_{\nu\mathbf{q}}$, we find the most influential phonon mode for the superconductivity and T_c. Fig. 4.4 shows the phonon dispersion of NaFeAs, NaCoAs and NaNiAs. In this figure, the magnitude of $\lambda_{\nu\mathbf{q}}$ is represented by radius of circle on each phonon dispersion.

The phonon band structure of NaCoAs is similar to that of NaFeAs, and the partial electron-phonon interaction, too. On the other hand, NaNiAs has lower frequency than the others. The low frequency of NaNiAs means the softness of the material. This softness and lattice instability is attributed to the occupation of the anti-bonding bands at Fermi level as shown in fig. 4.3.

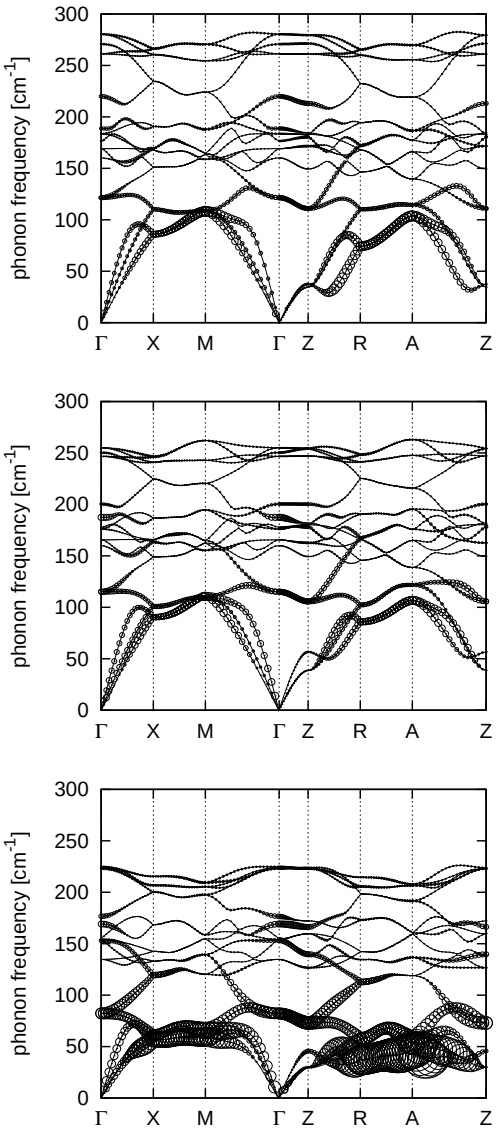

Figure 4.4: Phonon dispersions of NaFeAs(top), NaCoAs(center) and NaNiAs(bottom). The radius of circle displays the magnitude of partial electron-phonon interaction $\lambda_{\nu\mathbf{q}}$. The definition is explained in the section 2.3.3.

In NaNiAs, low frequency phonon modes have large electron-phonon interaction. These phonon modes expand and contract the covalent bondings of As and transition metal. Not only NaNiAs but also NaFeAs and NaCoAs have these phonon modes because the types of phonon modes are determined only by the lattice symmetry and the lattices of three materials are same. In spite of same phonon modes, why only NaNiAs has large electron-phonon interaction ? The difference is attributed to the bands at Fermi level. In NaNiAs, the electrons in anti-bonding bands at Fermi level can interact largely with the phonon modes because they are involved in bondings which are expanded and contracted by the phonons. As for NaFeAs and NaCoAs, the bands at Fermi level are the non-covalent bonding bands as seen in fig. 4.1.

4.4 Summary

In this chapter, we compared the electronic and phonon properties of NaFeAs, NaCoAs and NaNiAs. We find a realization of rigid band picture among three compounds. NaFeAs is semimetalic feature and has two-dimensional Fermi surface, while NaNiAs is metal and has three-dimensional Fermi surface. The NaNiAs has the largest electron-phonon interaction and the highest superconducting critical temperature, because some phonon modes expand and contract the covalent bondings of Ni and As. As for the NaFeAs and the NaCoAs, these modes do not have strong interaction because they have non-covalent bonding bands at Fermi level. From these findings, we conclude that it is important for the covalent bonding (or anti-bonding) bands to locate at Fermi level.

Chapter 5

$CuAlO_2$

5.1 $CuAlO_2$ under high pressure

5.1.1 Introduction

$CuAlO_2$, is known as p-type transparent conductor. The "p-type" transparent conductor is rare and important, because it is necessary for the p-n junction of the transparent conductors. Many appricaltions of $CuAlO_2$ are expected: flat panel displays, solar cells and the high-efficient thermo-electric-power materials, and so on.

Katayama-Yoshida and co-workers have calculated the Fermi surface of p-type doped $CuAlO_2$ by shifting the Fermi level rigidly.[46] The calculated Fermi surface is nesting, showing two-dimensional characteristics. These authors expected that the nesting Fermi surface may cause a strong electron-phonon interaction and a transparent superconductivity for visible light.

While they considered the p-type doped $CuAlO_2$, semiconductors can be metallized not only by doping, but also by pressure. As stated above, we are better informed about the pressure than the doping. In addition, the

pressured system is calculated more easily than the doped one. Therefore, first we consider the pressured $CuAlO_2$.

The purpose of this section is to clarify the stable structure and band gap of $CuAlO_2$ under high pressure and examine whether it is metallized or not by using first-principles calculations. Our results show that $CuAlO_2$ transforms to a leaning delafossite structure and that the energy gap rises and falls as pressure increases in both the structures.

5.1.2 Methods

First-principles calculations were performed within the density functional theory[10, 11] with a plane-wave pseudopotential method, as implemented in the Quantum-ESPRESSO code.[12] We employed the Perdew-Burke-Ernzerhof generalized gradient approximation exchange-correlation functional[36] and ultra-soft pseudopotentials.[14] For the pseudopotentials, Cu 3d electrons were also included in the valence electrons.

We used $16 \times 16 \times 4$(delafossite) and $8 \times 8 \times 4$(chalcopyrite) **k**-point grids. The energy cut-off for wave functions is 40 Ry and that for charge density is 320 Ry. This **k**-point meshes and cut-off energies are fine enough to achive convergence within 0.1mRy/atom in the total energy.

Atomic positions and cell parameters were optimized by the constant-pressure variable-cell relaxation using the Parrinello-Rahman method[15] without any symmetry requirements. Some materials similar to $CuAlO_2$($CuAlS_2$, $CuAlSe_2$, $CuAlTe_2$) have a chalcopyrite structure.[47] In order to research whether a chalcopyrite structure can appear under high pressure, we started optimization from not only delafossite, but also chalcopyrite structure. Initial cell parameters of the preliminary calculation are the experimental values at ambient pressure.[48]

$CuAlO_2$, has a delafossite structure at atmospheric pressure.[49] The unit cell of the delafossite structure is represented by a hexagonal cell or a rhombohedral cell. Fig. 5.1(a) shows the conventional hexagonal cell of $CuAlO_2$. For convenience, the hexagonal cell is used here.

5.1.3 Results and Discussion

Structural optimizations under high pressure

Under lower pressure, the local stable structure is delafossite structure and no structural transition is found. Under higher pressure, a new structure phase appears as a stable structure. Fig. 5.1(b) shows the hexagonal cell of this new structure. We call this structure a leaning delafossite structure because the crystal structure seems to be leaning.

Fig. 5.2 shows optimized cell parameters. At 60 GPa, lattice constant a increases slightly and c/a decreases. After the structural transition, angle α decreases from 90°, and oxygen atoms at $(0, 0, \pm z)$ move to $(\pm x, \pm 2x, \pm z)$. The other oxygen atoms at $(2/3, 1/3, \pm z + 1/3), (1/3, 2/3, \pm z + 2/3)$ move similarly. Table 5.1 shows our results and previous theoretical studies.[50, 51] Our results agree with the previous results well.

	0 GPa			30 GPa		
	a[Å]	c/a	z	a[Å]	c/a	z
This study	2.861	5.9690	0.1101	2.704	6.1670	0.1088
Ref.50	2.839	5.9331	0.1099	2.698	6.065	0.1089
Ref.51	2.835	5.999	0.11	2.713	6.2	0.1088

Table 5.1: Comparison of calculated cell parameters a,c/a and z with previous studies.[50, 51] Note that some parameters are not written explicitly in these papers. We read these parameters from the graphs.

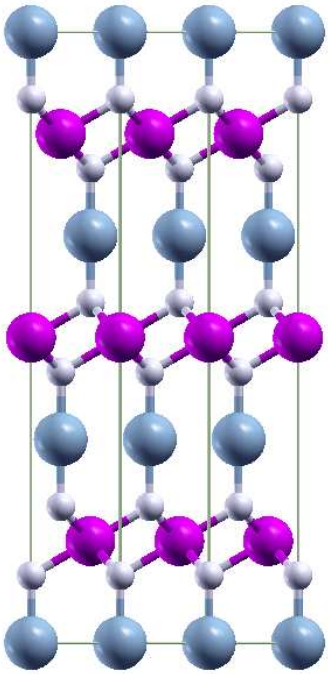

(a) delafossite structure.

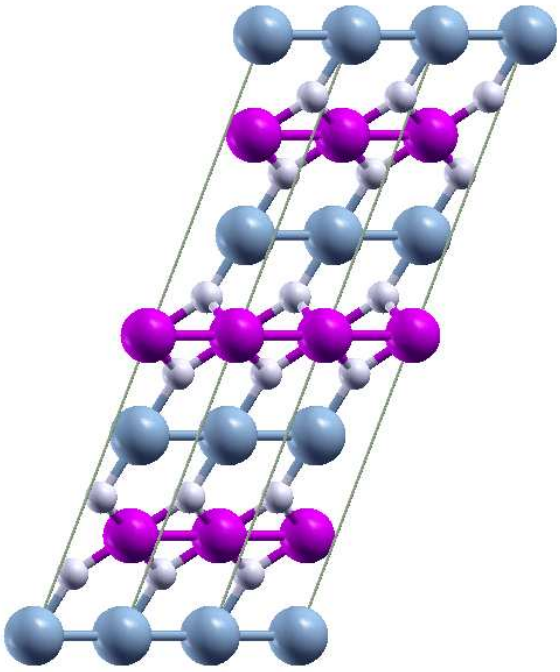

(b) leaning delafossite structure.

Figure 5.1: Side view of crystal cells. These cells contain Cu, O, and Al atom layers from the top.

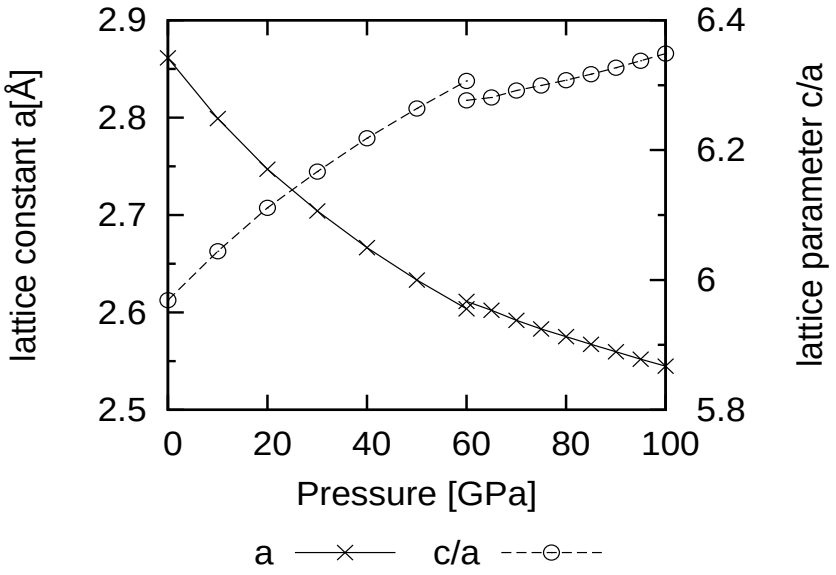

(a) lattice constant a and c/a.

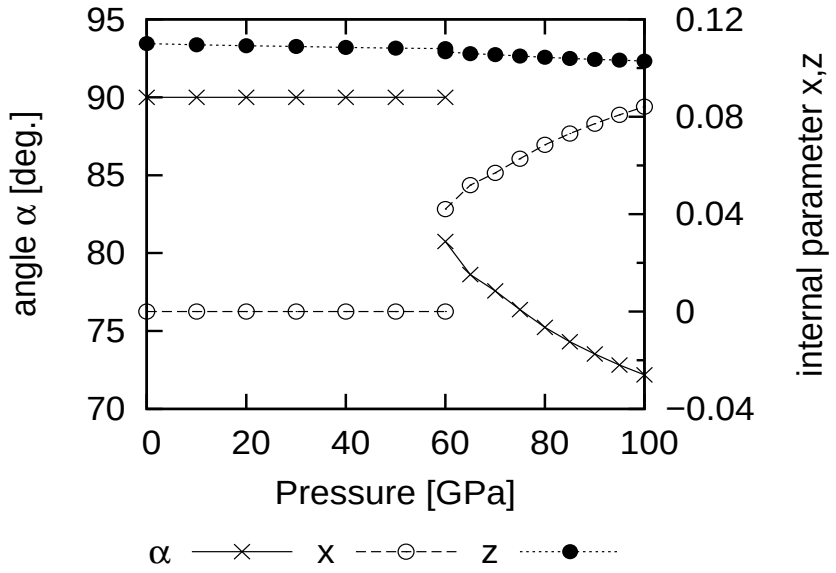

(b) angle α and internal parameters x and z.

Figure 5.2: Optimized lattice parameters.

Fig. 5.3 shows the enthalpies of delafossite, leaning delafossite, and chalcopyrite structures. Here, the enthalpy of the delafossite structure is set to be 0 Ry. The critical pressure of the structural transition from delafossite to leaning delafossite is 60 GPa. As pressure increases, the enthalpy of the chalcopyrite structure increases. Therefore, we conclude that under high pressure $CuAlO_2$ does not transform to the chalcopyrite structure. The result that no structural transition occurs under 20 GPa is consistent with experimental data.[52]

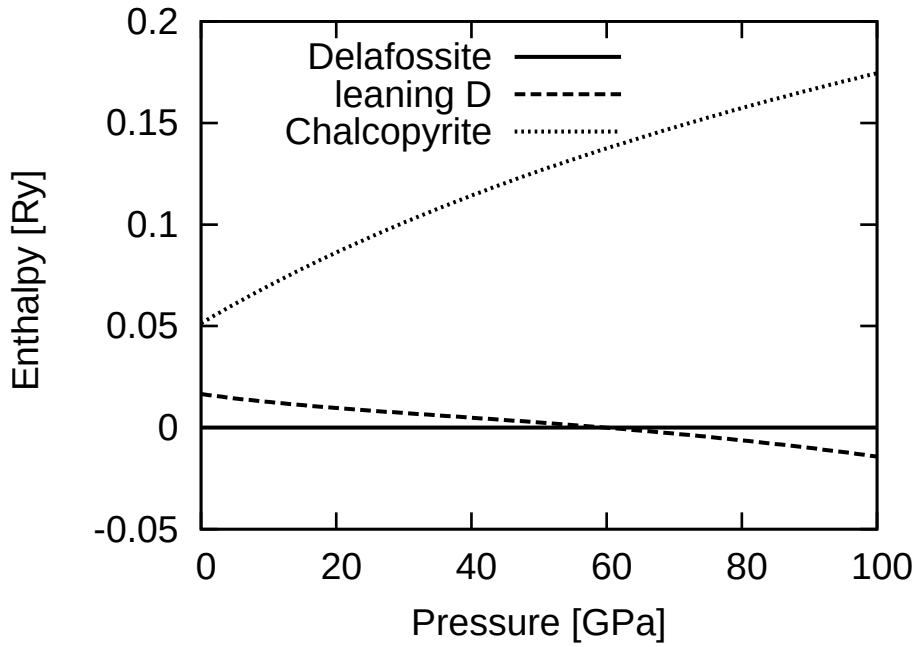

Figure 5.3: Enthalpies under high pressure. The enthalpy of delafossite structure is set to be 0 Ry.

Table 5.2 shows total energy, volume and enthalpy of delafossite and leaning delafossite structure at 100 GPa. The leaning delafossite structure has higher total energy than delafossite structure, though the former has lower enthalpy than later. On the other hand, the leaning delafossite structure

has smaller volume than delafossite structure. Therefore, the small volume leaning delafossite structure is important for stability under high pressure.

	Total energy [Ry]	Volume [a.u.^{3}]	enthalpy [Ry]
delafossite	-198.232535	198.1865	-196.885303
leaning delafossite	-198.197797	190.8753	-196.900758

Table 5.2: Total energy, volume and enthalpy of delafossite and leaning delafossite structure at 100 GPa.

Pressure dependence of the density of states and energy gap

Fig. 5.4 shows pressure dependence of the energy gap under high pressure. In both structure, the pressure dependence of the energy gap are same: rises and falls. At 60 GPa, the structural transition occurs and the energy gap jumps. In the pressure region from 0 GPa to 30 GPa, the calculated indirect energy gap follows as $E_g = 0.0149P + 1.84$[eV]. This pressure coefficient is consistent with experimental data.[52] From 30 GPa to 60 GPa, it follows as $E_g = -0.00343P + 2.37$ [eV].

The $CuAlO_2$ has a Cu $3d_{3z^2-r^2}$-O $2p_z$ anti-bonding state and a Cu $4p_{x,y}$ state as conduction bands. As pressure increases, the anti-bonding state rises because of the bonding length of O-Cu-O shorts. On the other hand, the band width of a Cu $4p_{x,y}$ state is extended. because the distance between Cu atoms decreases. As a result, a transition width between valence and conduction band is reduced. These two cometing pressure dependencies make the energy gap rises and falls.

Near 60 GPa, the energy gap decreases as pressure increases. As shown in Fig. 5.2(a), the structural transition expands lattice constant a. This reverse pressure effect is the reason why the energy gap jumps.

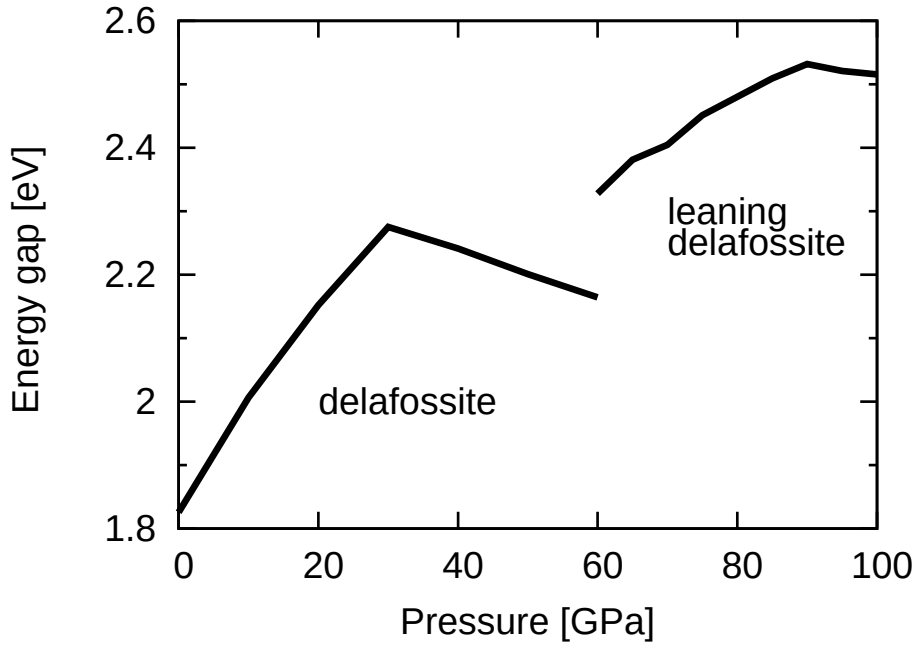

Figure 5.4: Pressure dependence of the energy gap under high pressure.

5.1.4 Summary

In this section, we calculated the stable structure of $CuAlO_2$ under high pressure and found that it transforms from the delafossite structure to the leaning delafossite structure at $P_c = 60$ GPa. On the other hand, a chalcopyrite structure is not found to be a stable structure. The energy gap rises and falls as pressure increases in both the structures. Through the structural transition, the energy gap is slightly expanded. The O-Cu-O dumbbell-like coupling is stable under high pressure.

5.2 Self-interaction correction

5.2.1 Introduction

Many first-principles calculations use local density approximation(LDA). The simplicity of the LDA enables fast calculation and, however, causes some errors. One of the faults is underestimation of energy gap. For example, E_g of $CuAlO_2$ is determined to be 1.84 eV by first-principle calculation as shown in the previous section, while the experimental data is 2.96 eV.[52] One reason of this error is the self-interaction in the energy functional. This is a Coulomb and exchange-correlation interaction between one electron and himself. This interaction is non-physical. For one-electron system, the sum of Coulomb, exchange and correlation energy should be zero. In the LDA, however, this is not always zero. The effect of non-zero self-interaction is small for itinerant systems. As for localized systems, however, it is not negligible and often cases some error.

Perdew and Zunger proposed the method for the self-interaction correction (SIC).[55] Their method is suitable for free atoms, but not for condensed systems due to a large computing effort. Vogel and co-workers suggested the alternative to Perdew's method and applied their approach to non-magnetic semiconductors.[54] Filippetti and Spaldin develop the Vogel's method.[53] Filippetti's approach can be applied to more general cases, in particular, to magnetic and highly correlated systems. In this study, we implemented Filippetti's method into first-principles calculation code, Quantum-espresso[12] and compared the energy gaps calculated within LDA and SIC.

In this section, we explained the formulation of the SIC and applied the SIC for typical semiconductor, GaN, and $CuAlO_2$.

5.2.2 Formulation

The useful SIC method is suggested by Perdew and Zunger.[55] It subtracts the self-interaction contribution from Hartree $E_{\rm h}[n]$ and exchange-correlation energy $E_{\rm xc}[n_\uparrow, n_\downarrow]$,

$$E_{\rm h}[n] + E_{\rm xc}[n_\uparrow, n_\downarrow] \rightarrow E_{\rm h}[n] + E_{\rm xc}[n_\uparrow, n_\downarrow] - \sum_{i\sigma}(E_{\rm h}[n_{i\sigma}] + E_{\rm xc}[n_{i\sigma}, 0]). \quad (5.1)$$

Here $n = n_\uparrow + n_\downarrow$ is the total electronic charge density, and $n_{i\sigma} = |\psi_{i\sigma}|^2$ is the density of an orbital with quantum numbers i and spin σ. In the self-interaction term, a single orbital is fully spin polarized. Minimizing the total energy including this term, they got one-electron equation:

$$\{-\nabla^2 + V_{\rm ext} + V_{\rm h}[n] + V_{\rm xc}[n_\uparrow, n_\downarrow] - V_{\rm h}[n_{i\sigma}] - V_{\rm xc}[n_{i\sigma}, 0]\}\psi_{i\sigma} = \epsilon_{i\sigma}\psi_{i\sigma}. \quad (5.2)$$

This method can improve total energies, ionization potentials, and electron affinities of atoms. However, the application for extended systems is difficult because self-interaction term of this approximation, $-V_{\rm h}[n_{i\sigma}] - V_{\rm xc}[n_{i\sigma}, 0]$, is orbital-dependent and vanishes as $\Omega^{-\frac{1}{3}}$ (Ω: the system volume).[55]

Vogel *et al.* improved this method by using self-interaction correlated pseudopotential and approximating the SI in the crystal with that in the free atom.[54] In this method, SIC is described by a non-local potential like the usual pseudopotential.

$$\{-\nabla^2 + V_{\rm ext} + V_{\rm hxc} - \sum_i |\phi_i > V_{\rm hxc}[n_{i\sigma}] < \phi_i|\}|\psi_{n\mathbf{k}\sigma} >= \epsilon_{n\mathbf{k}\sigma}|\psi_{n\mathbf{k}\sigma} > . \quad (5.3)$$

$$V_{\rm hxc}[n_{i\sigma}] = V_{\rm h}[n_{i\sigma}] + V_{\rm xc}[n_{i\sigma}, 0]. \quad (5.4)$$

Here, ϕ_i is the atomic orbitals. This method is efficient for some highly ionic compounds with atomic-like, poorly hybridized bands, such as II-VI semiconductors.

Filippetti and Spaldin generalized the Vogel's method.[53] They introduced the occupation numbers $p_{i\sigma}$.

$$n_{i\sigma} = p_{i\sigma}|\phi_i|^2 \tag{5.5}$$

$$p_{i\sigma} = \sum_{n\mathbf{k}} f_{n\mathbf{k}\sigma}| < \psi_{n\mathbf{k}\sigma}|\phi_i > |^2 \tag{5.6}$$

Vogel's method corresponds to that $p_{i\sigma}$ is 1. Introduction of $p_{i\sigma}$ make application for general cases: hybridized bands, magnetic system and metal.

For saving time, they approximated as the following:

$$V_{\rm hxc}[p_{i\sigma}|\phi_i|^2] \simeq p_{i\sigma}V_{\rm hxc}[|\phi_i|^2] \tag{5.7}$$

This is exact for the Hartree term. At each iteration of the self-consistency, you needs only recalculation of $p_{i\sigma}$ and not recalculation of $V_{\rm xc}[p_{i\sigma}|\phi_i|^2]$.

In this study, we started the formulation from the total energy. SIC-corrected total energy is as following:

$$E_{\rm tot} = \sum_{n\mathbf{k}\sigma} < \psi_{n\mathbf{k}\sigma}|[-\nabla^2 + V_{\rm ext}]|\psi_{n\mathbf{k}\sigma} > + E_{\rm hxc} - \sum_{i\sigma} E_{\rm hxc}[p_{i\sigma}|\phi_i|^2] \tag{5.8}$$

Minimizing this total energy, we got one-electron equation:

$$\{-\nabla^2 + V_{\rm ext} + V_{\rm hxc} - \sum_i |\phi_i > \quad C_i \quad < \phi_i|\}|\psi_{n\mathbf{k}\sigma} >= \epsilon_{n\mathbf{k}\sigma}|\psi_{n\mathbf{k}\sigma} > \tag{5.9}$$

$$C_i =< \phi_i|V_{\rm hxc}[p_{i\sigma}|\phi_i|^2]|\phi_i > \tag{5.10}$$

In addition, the approximation shown as (5.7) is applied

5.2.3 Methods

First-principles calculations were performed within the density functional theory[10, 11] with a plane-wave pseudopotential method, as implemented in the Quantum-ESPRESSO code.[12] We employed the Perdew-Wang type[13]

(GaN) and the Perdew-Burke-Ernzerhof type[36] ($CuAlO_2$) generalized gradient approximation exchange-correlation functional and ultra-soft pseudopotentials.[14] In electronic calculation, we used $8\times8\times8$ (GaN) and $8\times8\times2$ ($CuAlO_2$) **k**-point grid in the Monkhorst-Pack grid.[16] Energy cut-off for wave function is 40 Ry and that for charge density is 320 Ry.

5.2.4 Results and Discussion

Fig. 5.5 shows the band structures of GaN which are calculated within the LDA and the SIC. In the LDA (Fig. 5.5(a)), the Ga d bands locate at the same energy level as the N s bands and make a s-d hybridized band. This s-d hybridization splits the N s band. and push up the valence N p bands. As a result, the energy gap is underestimated: calculation results is $E_g = 1.88\,\mathrm{eV}$, while experimental data is $E_g = 3.5\,\mathrm{eV}$.[56]

In the SIC (Fig. 5.5(b)), the Ga d bands locate below the N s bands and does not make a s-d hybridized band. The energy gap is corrected: $E_g = 2.42$ eV.

Fig. 5.6 shows the band structures of $CuAlO_2$ which are calculated in LDA and SIC. In the band figure, there is no large difference between the LDA result (Fig. 5.6(a)) and the SIC result (Fig. 5.6(b)). But, the band width of the valence band in the SIC is narrower than that in the LDA. This is attributed to that the SIC makes the d-band potential more attractive. As a result, the energy gap of the SIC ($E_g = 3.16\,\mathrm{eV}$) is larger than that of the LDA ($E_g = 1.84\,\mathrm{eV}$) and close to experimental data ($E_g = 2.96\,\mathrm{eV}$[52]).

5.2.5 Summary

In this section, we calculated self-interaction correction by using first-principles calculations. The SIC expanded the energy gaps of GaN and $CuAlO_2$.

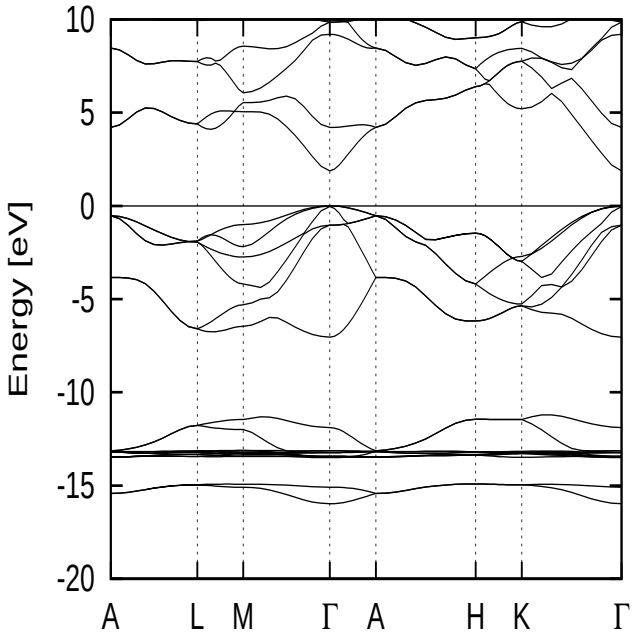

(a) Local density approximation

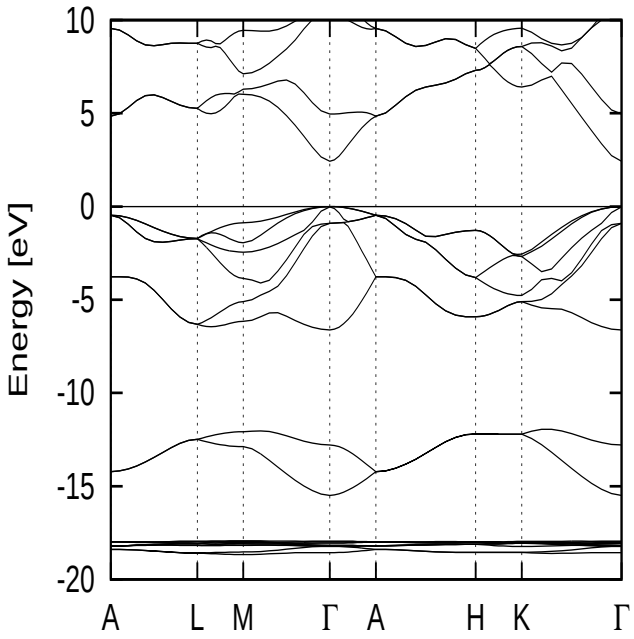

(b) Self-interaction correction

Figure 5.5: Band structure of wurtzite GaN.

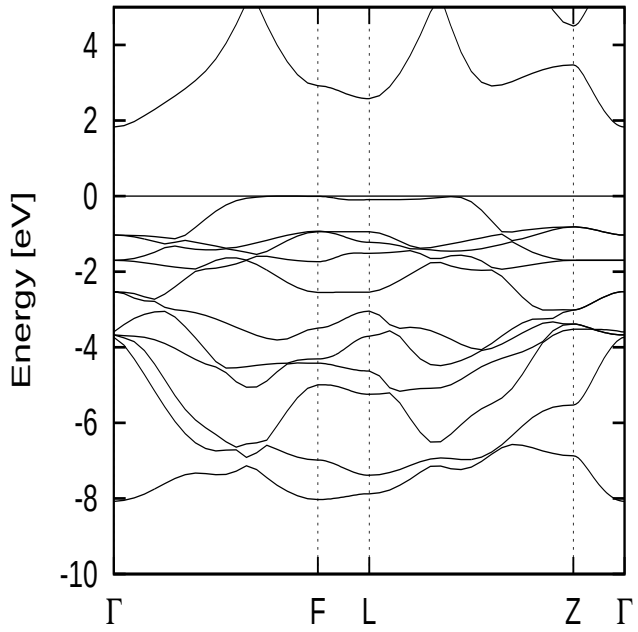

(a) Local density approximation

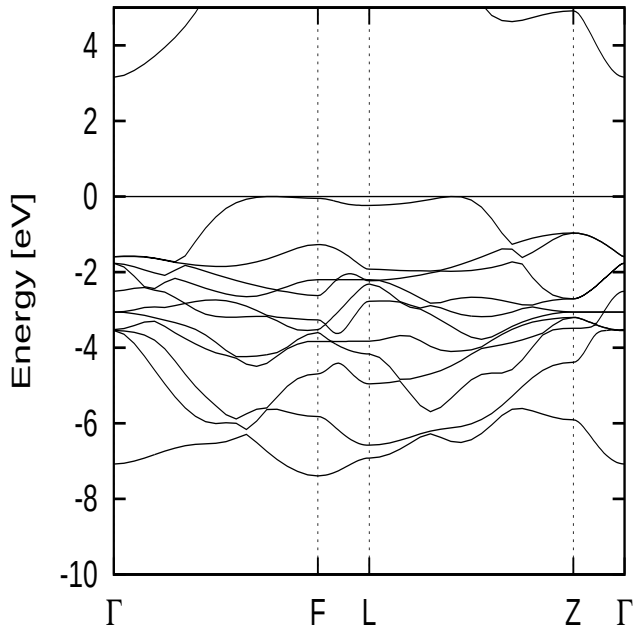

(b) Self-interaction correction

Figure 5.6: Band structure of CuAlO2.

5.3 Doped $CuAlO_2$

5.3.1 Introduction

As stated in section 5.1, Katayama-Yoshida, *et al.* have calculated the Fermi surface of p-type doped $CuAlO_2$ by shifting the Fermi level rigidly.[46] They speculated that the doped $CuAlO_2$ may be a transparent superconductivity for visible light. But, they only suggested the possibility and did not calculate the electron-phonon interaction and the critical temperature of the doped $CuAlO_2$.

The purpose of this section is to clarify the superconductivity of the doped $CuAlO_2$ by using first-principles calculations. Our results show that $0.1 \sim 0.2$ hole doped $CuAlO_2$ can be high temperature superconductor with $T_c \sim 40$K.

5.3.2 Methods

First-principles calculations were performed within the density functional theory[10, 11] with a plane-wave pseudopotential method, as implemented in the Quantum-ESPRESSO code.[12] We employed the Perdew-Burke-Ernzerhof generalized gradient approximation exchange-correlation functional[36] and ultra-soft pseudopotentials.[14] For the pseudopotentials, Cu 3d electrons were also included in the valence electrons. Therefore, non-doped $CuAlO_2$ has 26 electrons. In this study, we calculated $CuAlO_2$ with number of electron $N_{el} = 25.0 \sim 25.8$. A calculation with $N_{el} = 25.9$ does not convergence.

In electronic and phonon calculation, we used $8 \times 8 \times 8$ **k**-point grid in the Monkhorst-Pack grid.[16] Energy cut-off for wave function is 40 Ry and that for charge density is 320 Ry. These **k**-point meshes and cut-off energies are fine enough to achieve convergence within 0.1mRy/atom in the total energy.

We used the optimization results in section 5.1 as inputs.

We explain how to calculate the doped $CuAlO_2$. It is difficult to calculate the property of doped system exactly. Therefore, some properties are approximately calculated in this study. Let us pick up the electron-phonon interaction λ as an example. This is represented as following.

$$\lambda = \sum_{\nu\mathbf{q}} \frac{2N(\varepsilon_{\mathrm{F}}) \sum_{\mathbf{k}} |M^{\nu\mathbf{q}}_{\mathbf{k},\mathbf{k}+\mathbf{q}}|^2 \delta(\varepsilon_{\mathbf{k}} - \varepsilon_{\mathrm{F}}) \delta(\varepsilon_{\mathbf{k}+\mathbf{q}} - \varepsilon_{\mathrm{F}})}{\omega_{\nu\mathbf{q}} \sum_{\mathbf{k}\mathbf{q}'} \delta(\varepsilon_{\mathbf{k}} - \varepsilon_{\mathrm{F}}) \delta(\varepsilon_{\mathbf{k}+\mathbf{q}'} - \varepsilon_{\mathrm{F}})}. \tag{5.11}$$

In the calculation of electron-phonon interaction, averaging at Fermi surface are performed. We shifted the Fermi level ε_{F} rigidly in the averaging. On the other hand, the electron-phonon matrix $M^{\nu\mathbf{q}}_{\mathbf{k},\mathbf{k}+\mathbf{q}}$ and the phonon frequency $\omega_{\nu\mathbf{q}}$ of non-doped $CuAlO_2$ are used. The idea underlying this approximation is that doping does not greatly change the whole band structure of the electron and the phonon.

5.3.3 Results and Discussion

Electronic band structure

Fig. 5.7 shows the electronic density of states(DOS) of non-doped $CuAlO_2$. The valence band of $CuAlO_2$ has a small peak. This peak is mainly occupied by a Cu $3d_{3z^2-r^2}$-O $2p_z$ anti-bonding state.

Fig.5.8 tells us the corresponds of the Fermi level to number of electrons. When $N_{\mathrm{el}} = 25.7$, Fermi level locates at the top of the small peak. When $N_{\mathrm{el}} = 25.4$, Fermi level locates at the valley of DOS.

Superconducting critical temperature

Fig. 5.9 shows the superconducting critical temperature. Note that the x-axis is not doping concentration, but the number of electrons. When $\mathrm{N_{el}} = 25.7 \sim 25.8$, $CuAlO_2$ has $T_{\mathrm{c}} \simeq 40\,\mathrm{K}$. Especially, superconducting critical

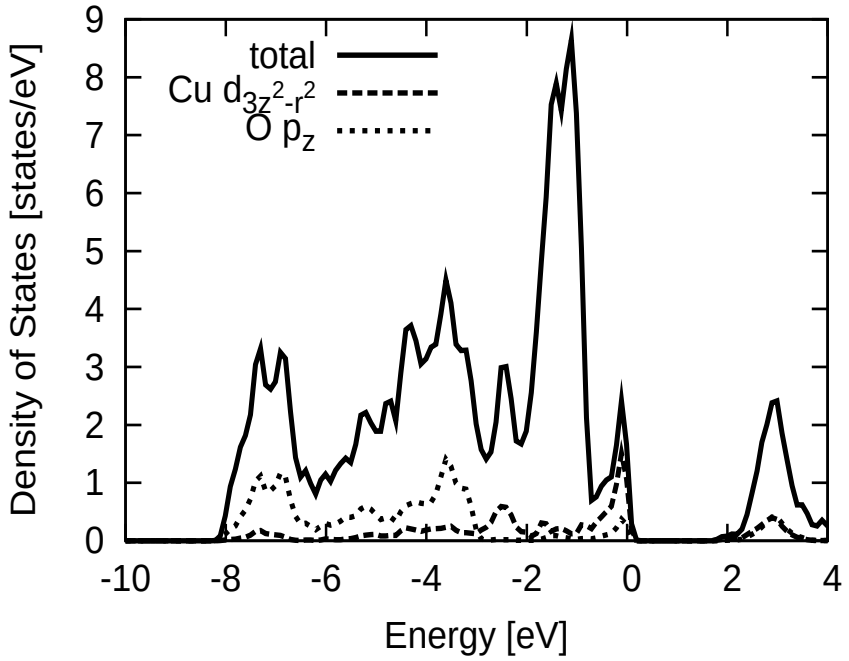

Figure 5.7: Total and partial density of states.

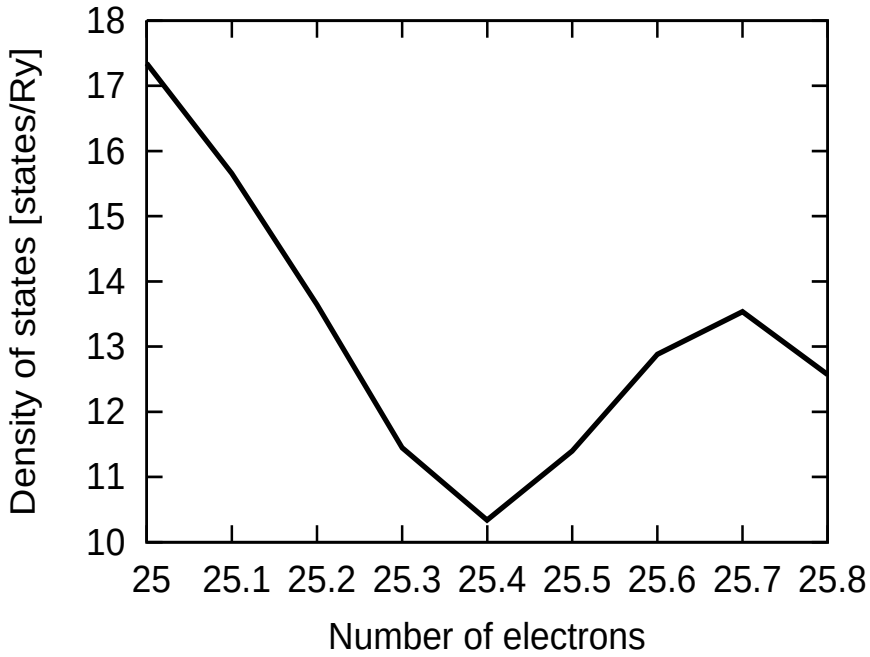

Figure 5.8: Density of states at the Fermi level.

temperature of 0.2 hole-doped $CuAlO_2$, $T_c = 44$ K, is the highest record among phonon-mediated superconductors. The heavily-doped $CuAlO_2$($N_{el} = 25.0 \sim 25.4$), however, has $T_c \simeq 10\,\mathrm{K}$.

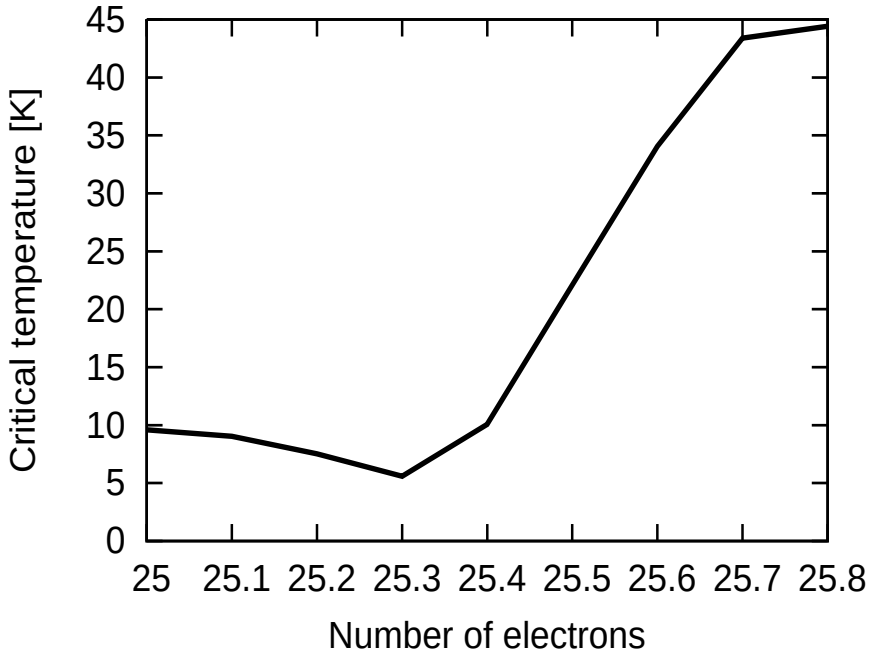

Figure 5.9: Superconducting critical temperature

Let us examine the origin of the high T_c of lighter-doped $CuAlO_2$ ($N_{el} = 25.7 \sim 25.8$). According to the Allen-Dynes modified McMillan's formula,[24, 25] T_c is given by three factors: the electron-phonon interaction λ, the logarithmic averaged phonon frequency ω_{log}, and the screened Coulomb interaction μ^*, in the following form.

$$T_c = \frac{\omega_{log}}{1.2} \exp\left(-\frac{1.04(1+\lambda)}{\lambda - \mu^*(1+0.62\lambda)}\right). \tag{5.12}$$

Here λ and ω_{log} are obtained by the first-principle calculations using the density functional perturbation theory. As for μ^*, we assume the value $\mu^* \simeq 0.1$. This value holds for weak correlated systems. In this study, the critical

temperature is determined by λ and $\omega_{\log}$. The table 5.3 shows λ and $\omega_{\log}$. When $N_{\rm e}$ increases, λ rises about 90%, while $\omega_{\log}$ rises about 10%. Therefore, the large λ leads to the high $T_{\rm c}$.

$N_{\rm el}$	λ	$\omega_{\log}$ [K]
25.3	0.449	727
25.8	0.870	806

Table 5.3: Electron-phonon interaction λ and logarithmic averaged phonon frequencies $\omega_{\log}$. $T_{\rm c}$ has max. and min. at $N_{\rm el} = 25.8, 25.3$.

Here we analyze the electron-phonon interaction. For the mode analysis, we introduce partial electron-phonon interaction $\lambda_{\nu\mathbf{q}}$ so that $\lambda = \sum \lambda_{\nu\mathbf{q}}$ as same as section 2. Using $\lambda_{\nu\mathbf{q}}$ we find the most influential phonon mode for the superconductivity and $T_{\rm c}$. In Fig. 5.10, the magnitude of $\lambda_{\nu\mathbf{q}}$ is represented by radius of circle on each phonon dispersion. According to this figure, the highest mode on the $Z - \Gamma$ line has large electron-phonon interaction. This mode is called the A_1L_1 mode. In this mode, the O atoms oscillate in the anti-phase and the oscillation direction is parallel to a O-Cu-O bond.

Irrespective of $N_{\rm el}$, $CuAlO_2$ has an A_1L_1 mode because the types of phonon modes are determined only by the lattice symmetry. In spite of the same phonon mode, why only lighter-doped $CuAlO_2$ has large electron-phonon interaction ? The difference is attributed to the bands at Fermi level. In the case with $N_{\rm el} = 25.7 \sim 25.8$, the Cu $3d_{3z^2-r^2}$ and the O $2p_z$ electrons appears at Fermi level and make O-Cu-O covalent bond. They have large interaction with the A_1L_1 mode phonon because a bonding direction is parallel to an oscillation direction of the A_1L_1 mode phonon. As $N_{\rm el}$ decreases, the electron-phonon interaction decreases, due to reduction of Cu $3d_{3z^2-r^2}$

and the O $2p_z$ electrons, which strongly interact with A_1L_1 phonon.

5.3.4 Summary

In this section, we calculated the superconducting critical temperature of hole-doped $CuAlO_2$ by using first-principles calculations. In lightly hole-doped $CuAlO_2$, Cu $3d_{3z^2-r^2}$ and O $2p_z$ electrons appear at the Fermi level. A_1L_1 phonon mode have a strong interaction with these electrons because the oscillation direction of this mode is parallel to the bonding direction of these electrons. Based on these findings, we conclude that lightly hole-doped $CuAlO_2$ can be high T_c superconductor.

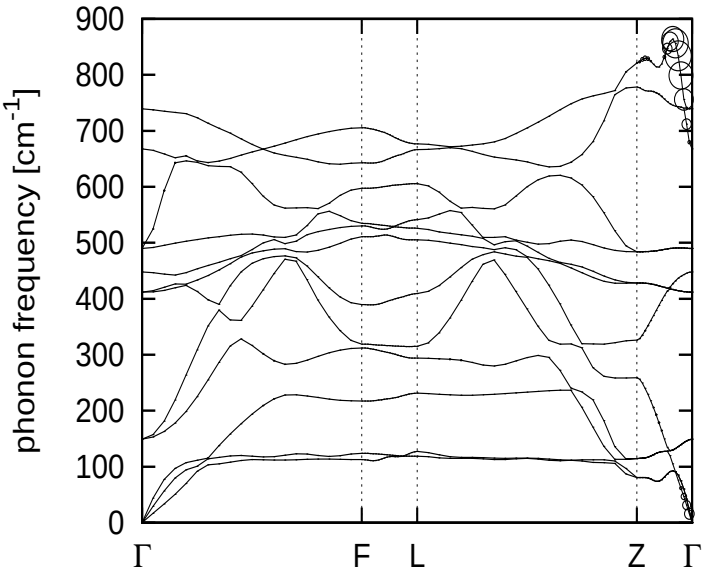

(a) Number of electrons is 25.3

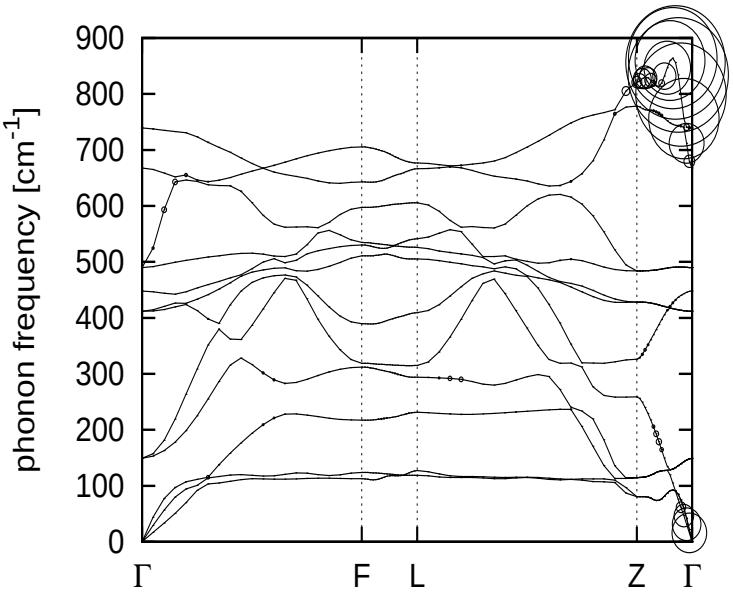

(b) Number of electrons is 25.8

Figure 5.10: Phonon dispersions and electron-phonon interactions of doped $CuAlO_2$. The radius of circle displays the magnitude of partial electron-phonon interaction $\lambda_{\nu\mathbf{q}}$. The definition is explained in the text.

Chapter 6

Conclusion of this thesis

The strong coupling theory enables us to quantitatively calculate the superconducting critical temperature of phonon-mediated superconductors. This is useful for the prediction of critical temperature under unresearched condition and the determination of whether the material is phonon-mediated superconductors. In this study, we predicted the critical temperature of $CaSi_2$ in AlB_2 structure, phosphorus in incommensurate structure, NaCoAs, NaNiAs, and doped $CuAlO_2$. In addition, we determined NaFeAs is not phonon-mediated superconductor by comparing results of electron-phonon calculation with experimental data.

In $CaSi_2$ and $CuAlO_2$, the directions of phonon oscillation and electronic bonding are important for the superconductivity. When these directions agree, the electron-phonon interaction and the critical temperature increase. In addition, as stated in chapter of NaFeAs and $CuAlO_2$, it is also important that the covalent bonding bands locate at the Fermi level, because the covalent bondings make the hard lattice and this makes the strong electron-phonon interaction.

The results of this thesis suggest two policies: 1)The direction of covalent

bonding agrees with that of the lattice oscillation and 2)The covalent bonding bands locate at Fermi level. Following these policies, we will be able to design the superconductor with higher T_c.

Chapter 7

Acknowledgements

I thanks my collaborators, Professor Yoshida, Associate Professor Kusakabe, Dr. Nagara and Dr. Ishikawa. Professor. Yoshida is my supervisor and gave me the subject of $CuAlO_2$. Associate Professor Kusakabe gave me the subject of $CaSi_2$ and FeAs superconductors. Discussions with Professor Yoshida and Associate Professor Kusakabe have been insightful. Dr. Nagara gave me the subject of phosphorus. Dr. Nagara and Dr. Ishikawa taught me their knowledge of high pressure physics. I would like to express my gratitude to all members of Yoshida and Kusakabe laboratory and my family for their support and encouragement.

The authors acknowledge the financial support from the Global Center of Excellence program "Core Research and Engineering of Advanced Materials - Interdisciplinary Education Center for Materials Science", the Ministry of Education, Culture, Sports, Science and Technology, Japan, and a Grant-in-Aid for Scientific Research on Innovative Areas "Materials Design through Computics: Complex Correlation and Nano- Equilibrium Dynamics".

Appendix A

Strong coupling theory

We write the strong coupling theory of superconductor and explain how to calculate the superconducting critical temperature. In this chapter, Hartree atomic unit is employed and Boltzmann constant $k_B = 1$.

A.1 Eliashberg equation

In this section, we show the formulation of Eliashberg equation. The Eliashberg equation is an expansion of Dyson equation of normal-conductivity for superconductivity.

Within the first order approximation of ion displacement, the Hamiltonian which represents the electron-phonon interaction is as follows.

$$H_{\mathrm{el-ph}} = \sum_{\boldsymbol{k}\boldsymbol{q}\sigma} M_{\boldsymbol{k}+\boldsymbol{q},\boldsymbol{k}}(a_{\boldsymbol{q}} + a^{\dagger}_{-\boldsymbol{q}})c^{\dagger}_{\boldsymbol{k}+\boldsymbol{q}\sigma}c_{\boldsymbol{k}\sigma}. \tag{A.1}$$

Here, $c^{\dagger}_{\boldsymbol{k}\sigma}$ and $c_{\boldsymbol{k}\sigma}$ are creation and annihilation operators of electrons with wave number vector $\boldsymbol{k}$ and spin σ [1] and $a^{\dagger}_{\boldsymbol{q}}$ and $a_{\boldsymbol{q}}$ are creation and an-

[1] band index i is included in wave number vector $\boldsymbol{k}$ and omitted.

nihilation operators of phonons with wave number vector $\boldsymbol{q}$. [2] We define $\phi_{\boldsymbol{q}} \equiv (a_{\boldsymbol{q}} + a^{\dagger}_{-\boldsymbol{q}})$.

$M_{\boldsymbol{k}+\boldsymbol{q},\boldsymbol{k}}$ is the electron-phonon interaction when an electron is scattered from $\boldsymbol{k}$ to $\boldsymbol{k}+\boldsymbol{q}$ by a phonon with $\boldsymbol{q}$.

$$M_{\boldsymbol{k}+\boldsymbol{q},\boldsymbol{k}} = \frac{1}{\sqrt{2N_{\rm cell}M\omega_{\boldsymbol{q}}}}\langle \boldsymbol{k}+\boldsymbol{q}|\mathbf{n}_{\boldsymbol{q}}\cdot\nabla U|\boldsymbol{k}\rangle. \tag{A.2}$$

$N_{\rm cell}$ is a number of unit cell, M is a mass of ion, $\omega_{\boldsymbol{q}}$ is frequency of phonon, U is an ion potential and $\mathbf{n}_{\boldsymbol{q}}$ is a polarization vector of phonon.

The total Hamiltonian is as follows.

$$\mathcal{H} = \sum_{\boldsymbol{k}\sigma}\xi_{\boldsymbol{k}}c^{\dagger}_{\boldsymbol{k}\sigma}c_{\boldsymbol{k}\sigma} + \sum_{\boldsymbol{q}}\omega_{\boldsymbol{q}}a^{\dagger}_{\boldsymbol{q}}a_{\boldsymbol{q}} + \sum_{\boldsymbol{k}\boldsymbol{q}\sigma}M_{\boldsymbol{k}+\boldsymbol{q},\boldsymbol{k}}\phi_{\boldsymbol{q}}c^{\dagger}_{\boldsymbol{k}+\boldsymbol{q}\sigma}c_{\boldsymbol{k}\sigma}. \tag{A.3}$$

$\xi_{\boldsymbol{k}}$ is the energy of the electron. The electron Green's function is as follows.

$$\begin{aligned} & G(\boldsymbol{k},\tau-\tau') \\ \equiv\ & -\langle T c_{\boldsymbol{k}\uparrow}(\tau)c^{\dagger}_{\boldsymbol{k}\uparrow}(\tau')\rangle \\ =\ & -\langle c_{\boldsymbol{k}\uparrow}(\tau)c^{\dagger}_{\boldsymbol{k}\uparrow}(\tau')\theta(\tau-\tau') - c_{\boldsymbol{k}\uparrow}(\tau')^{\dagger}c_{\boldsymbol{k}\uparrow}(\tau)\theta(\tau'-\tau)\rangle. \end{aligned} \tag{A.4}$$

Here, $\langle A\rangle$ is a thermal average of A. When we set β reverse temperature,

$$\langle A\rangle = \frac{tr(e^{-\beta\mathcal{H}}A)}{tr(e^{-\beta\mathcal{H}})}. \tag{A.5}$$

T is the operator of time ordered product. The following holds for operators $A(\tau)$ and $B(\tau')$,

[2] phonon mode index ν is included in wave number vector $\boldsymbol{q}$ and omitted.

$$TA(\tau)B(\tau') = \begin{cases} A(\tau)B(\tau') & (\tau > \tau'), \\ \mp B(\tau')A(\tau) & (\tau' > \tau), \end{cases} \tag{A.6}$$

(−:Fermion, +:Boson). Here, $A(\tau) \equiv e^{\mathcal{H}\tau} A e^{-\mathcal{H}\tau}$. For getting the equation of motion for Green's function, we differentiate the Green's function by τ,

$$\frac{\partial}{\partial\tau} G(\boldsymbol{k}, \tau - \tau') = -\langle \delta(\tau - \tau')[c_{\boldsymbol{k}\uparrow}(\tau), c^\dagger_{\boldsymbol{k}\uparrow}(\tau')] + T[\mathcal{H}, c_{\boldsymbol{k}\uparrow}(\tau)] c^\dagger_{\boldsymbol{k}\uparrow}(\tau') \rangle. \tag{A.7}$$

Here,

$$\begin{aligned} [\mathcal{H}, c_{\boldsymbol{k}\uparrow}(\tau)] &= e^{\mathcal{H}\tau}[\mathcal{H}, c_{\boldsymbol{k}\uparrow}] e^{-\mathcal{H}\tau} \\ &= e^{\mathcal{H}\tau} \sum_{\boldsymbol{k}'\sigma} \xi_{\boldsymbol{k}'} [c^\dagger_{\boldsymbol{k}'\sigma} c_{\boldsymbol{k}'\sigma}, c_{\boldsymbol{k}\uparrow}] e^{-\mathcal{H}\tau} \\ &\quad + e^{\mathcal{H}\tau} \sum_{\boldsymbol{k}'\boldsymbol{q}\sigma} M_{\boldsymbol{k}'+\boldsymbol{q},\boldsymbol{k}'}\, \phi_{\boldsymbol{q}} [c^\dagger_{\boldsymbol{k}'+\boldsymbol{q}\sigma} c_{\boldsymbol{k}'\sigma}, c_{\boldsymbol{k}\uparrow}] e^{-\mathcal{H}\tau} \\ &= -e^{\mathcal{H}\tau} \xi_{\boldsymbol{k}} c_{\boldsymbol{k}\uparrow} e^{-\mathcal{H}\tau} - e^{\mathcal{H}\tau} \sum_{\boldsymbol{q}} M_{\boldsymbol{k},\boldsymbol{k}-\boldsymbol{q}} \phi_{\boldsymbol{q}} c_{\boldsymbol{k}-\boldsymbol{q}\uparrow} e^{-\mathcal{H}\tau} \\ &= -\xi_{\boldsymbol{k}} c_{\boldsymbol{k}\uparrow}(\tau) - \sum_{\boldsymbol{q}} M_{\boldsymbol{k},\boldsymbol{k}-\boldsymbol{q}} \phi_{\boldsymbol{q}}(\tau) c_{\boldsymbol{k}-\boldsymbol{q}\uparrow}(\tau). \end{aligned} \tag{A.8}$$

In addition, if we change $-\boldsymbol{q} \to \boldsymbol{q}$ and assume $\phi_{-\boldsymbol{q}} = \phi_{\boldsymbol{q}}$, (A.7) becomes as follows.

$$\begin{aligned} \frac{\partial}{\partial\tau} G(\boldsymbol{k}, \tau - \tau') &= -\delta(\tau - \tau') + \xi_{\boldsymbol{k}} \langle T c_{\boldsymbol{k}\uparrow}(\tau) c^\dagger_{\boldsymbol{k}\uparrow}(\tau') \rangle \\ &\quad + \sum_{\boldsymbol{q}} M_{\boldsymbol{k},\boldsymbol{k}+\boldsymbol{q}} \langle T \phi_{\boldsymbol{q}}(\tau) c_{\boldsymbol{k}+\boldsymbol{q}\uparrow}(\tau) c^\dagger_{\boldsymbol{k}\uparrow}(\tau') \rangle. \end{aligned} \tag{A.9}$$

Here, we define

$$\Gamma(\boldsymbol{q}, \boldsymbol{k}, \tau, \tau'', \tau') \equiv -\langle T \phi_{\boldsymbol{q}}(\tau) c_{\boldsymbol{k}+\boldsymbol{q}\uparrow}(\tau'') c^\dagger_{\boldsymbol{k}\uparrow}(\tau') \rangle. \tag{A.10}$$

and rewrite as follows.

$$\left[-\frac{\partial}{\partial\tau}-\xi_{\boldsymbol{k}}\right]G(\boldsymbol{k},\tau-\tau')=\delta(\tau-\tau')+\sum_{\boldsymbol{q}}M_{\boldsymbol{k},\boldsymbol{k}+\boldsymbol{q}}\Gamma(\boldsymbol{q},\boldsymbol{k},\tau,\tau,\tau'). \quad \text{(A.11)}$$

Next, in order to get the expression of Γ, we calculate the equation of motion for Γ.

In the preparation, we calculate the equations of motion for $a^\dagger_{\boldsymbol{q}}$, $a_{-\boldsymbol{q}}$ and $\phi_{\boldsymbol{q}}$. We differentiate $a^\dagger_{\boldsymbol{q}}$ by τ.

$$\begin{aligned}
\frac{\partial}{\partial\tau}a^\dagger_{\boldsymbol{q}}(\tau) &= [\mathcal{H},a^\dagger_{\boldsymbol{q}}(\tau)] \\
&= e^{\mathcal{H}\tau}[\mathcal{H},a^\dagger_{\boldsymbol{q}}]e^{-\mathcal{H}\tau} \\
&= e^{\mathcal{H}\tau}\sum_{\boldsymbol{q}'}\omega_{\boldsymbol{q}'}[a^\dagger_{\boldsymbol{q}'}a_{\boldsymbol{q}'},a^\dagger_{\boldsymbol{q}}]e^{-\mathcal{H}\tau} \\
&\quad +e^{\mathcal{H}\tau}\sum_{\boldsymbol{k}\boldsymbol{q}'\sigma}M_{\boldsymbol{k}+\boldsymbol{q}',\boldsymbol{k}}[(a_{\boldsymbol{q}'}+a^\dagger_{-\boldsymbol{q}'}),a^\dagger_{\boldsymbol{q}}]c^\dagger_{\boldsymbol{k}+\boldsymbol{q}\sigma}c_{\boldsymbol{k}\sigma}e^{-\mathcal{H}\tau} \\
&= e^{\mathcal{H}\tau}\omega_{\boldsymbol{q}}a^\dagger_{\boldsymbol{q}}e^{-\mathcal{H}\tau}+e^{\mathcal{H}\tau}\sum_{\boldsymbol{k}\sigma}M_{\boldsymbol{k}+\boldsymbol{q},\boldsymbol{k}}c^\dagger_{\boldsymbol{k}+\boldsymbol{q}\sigma}c_{\boldsymbol{k}\sigma}e^{-\mathcal{H}\tau} \\
&= \omega_{\boldsymbol{q}}a^\dagger_{\boldsymbol{q}}(\tau)+\sum_{\boldsymbol{k}\sigma}M_{\boldsymbol{k}+\boldsymbol{q},\boldsymbol{k}}c^\dagger_{\boldsymbol{k}+\boldsymbol{q}\sigma}(\tau)c_{\boldsymbol{k}\sigma}(\tau). \qquad \text{(A.12)}
\end{aligned}$$

As for $a_{\boldsymbol{q}}$, we calculate in a similar way.

$$\frac{\partial}{\partial\tau}a_{\boldsymbol{q}}(\tau) = -\omega_{\boldsymbol{q}}a_{\boldsymbol{q}}(\tau)-\sum_{\boldsymbol{k}\sigma}M_{\boldsymbol{k}-\boldsymbol{q},\boldsymbol{k}}c^\dagger_{\boldsymbol{k}-\boldsymbol{q}\sigma}(\tau)c_{\boldsymbol{k}\sigma}(\tau). \qquad \text{(A.13)}$$

In this formula, if we exchange $\boldsymbol{q}\to-\boldsymbol{q}$, assume $\omega_{-\boldsymbol{q}}=\omega_{\boldsymbol{q}}$ and rearrange the expression, the equations of motion for $a^\dagger_{\boldsymbol{q}}$ and $a_{-\boldsymbol{q}}$ become as follows.

$$\left[\frac{\partial}{\partial\tau}-\omega_{\boldsymbol{q}}\right]a^\dagger_{\boldsymbol{q}}(\tau) = \sum_{\boldsymbol{k}\sigma}M_{\boldsymbol{k}+\boldsymbol{q},\boldsymbol{k}}c^\dagger_{\boldsymbol{k}+\boldsymbol{q}\sigma}(\tau)c_{\boldsymbol{k}\sigma}(\tau), \qquad \text{(A.14)}$$

$$\left[\frac{\partial}{\partial\tau}+\omega_{\boldsymbol{q}}\right]a_{-\boldsymbol{q}}(\tau) = -\sum_{\boldsymbol{k}\sigma}M_{\boldsymbol{k}+\boldsymbol{q},\boldsymbol{k}}c^\dagger_{\boldsymbol{k}+\boldsymbol{q}\sigma}(\tau)c_{\boldsymbol{k}\sigma}(\tau). \qquad \text{(A.15)}$$

If we apply $[\frac{\partial}{\partial\tau}+\omega_{\boldsymbol{q}}]$ to (A.14), apply $[\frac{\partial}{\partial\tau}-\omega_{\boldsymbol{q}}]$ to (A.15) and sum up these, we obtain [3]

$$\left[\frac{\partial^2}{\partial\tau^2}-\omega_{\boldsymbol{q}}^2\right]\phi_{\boldsymbol{q}}(\tau) \;=\; 2\omega_{\boldsymbol{q}}\sum_{\boldsymbol{k}\sigma}M_{\boldsymbol{k}+\boldsymbol{q},\boldsymbol{k}}c^\dagger_{\boldsymbol{k}+\boldsymbol{q}\sigma}(\tau)c_{\boldsymbol{k}\sigma}(\tau), \tag{A.16}$$

From this formula and (A.10), we calculate the equation of motion for Γ.

$$\begin{aligned}&\left[\frac{\partial^2}{\partial\tau^2}-\omega_{\boldsymbol{q}}^2\right]\Gamma(\boldsymbol{q},\boldsymbol{k},\tau,\tau'',\tau')\\ =\;& -2\omega_{\boldsymbol{q}}\sum_{\boldsymbol{k}'\sigma}M_{\boldsymbol{k}'+\boldsymbol{q},\boldsymbol{k}'}\langle Tc^\dagger_{\boldsymbol{k}'+\boldsymbol{q}\sigma}(\tau)c_{\boldsymbol{k}'\sigma}(\tau)c_{\boldsymbol{k}+\boldsymbol{q}\uparrow}(\tau'')c^\dagger_{\boldsymbol{k}\uparrow}(\tau')\rangle.\end{aligned} \tag{A.17}$$

We use the phonon Green's function to solve this equation. The phonon Green's function is as follows.

$$D(\boldsymbol{q},\tau-\tau') \;\equiv\; -\langle T\phi_{\boldsymbol{q}}(\tau)\phi_{-\boldsymbol{q}}(\tau')\rangle. \tag{A.18}$$

This yields the equation of motion for phonon Green's function. If we differentiate the phonon Green's function by τ twice,

$$\begin{aligned}&\frac{\partial}{\partial\tau}D(\boldsymbol{q},\tau-\tau')\\ =\;& -\frac{\partial}{\partial\tau}\langle\phi_{\boldsymbol{q}}(\tau)\phi_{-\boldsymbol{q}}(\tau')\theta(\tau-\tau')+\phi_{-\boldsymbol{q}}(\tau')\phi_{\boldsymbol{q}}(\tau)\theta(\tau'-\tau)\rangle\\ =\;& -\langle T\frac{\partial\phi_{\boldsymbol{q}}}{\partial\tau}\phi_{-\boldsymbol{q}}(\tau')\rangle-\langle[\phi_{\boldsymbol{q}}(\tau),\phi_{-\boldsymbol{q}}(\tau')]\rangle\delta(\tau-\tau')\\ =\;& -\langle T\frac{\partial\phi_{\boldsymbol{q}}}{\partial\tau}\phi_{-\boldsymbol{q}}(\tau')\rangle,\end{aligned} \tag{A.19}$$

$$\begin{aligned}&\frac{\partial^2}{\partial\tau^2}D(\boldsymbol{q},\tau-\tau')\\ =\;& -\langle T\frac{\partial^2\phi_{\boldsymbol{q}}}{\partial\tau^2}\phi_{-\boldsymbol{q}}(\tau')\rangle-\langle[\frac{\partial\phi_{\boldsymbol{q}}}{\partial\tau},\phi_{-\boldsymbol{q}}(\tau')]\rangle\delta(\tau-\tau')\\ =\;& -\omega_{\boldsymbol{q}}^2\langle T\phi_{\boldsymbol{q}}(\tau)\phi_{-\boldsymbol{q}}(\tau')\rangle-2\omega_{\boldsymbol{q}}\sum_{\boldsymbol{k}\sigma}M_{\boldsymbol{k}+\boldsymbol{q},\boldsymbol{k}}\langle Tc^\dagger_{\boldsymbol{k}+\boldsymbol{q}\sigma}(\tau)c_{\boldsymbol{k}\sigma}(\tau)\phi_{-\boldsymbol{q}}(\tau')\rangle\\ &-\omega_{\boldsymbol{q}}\langle[\left(a^\dagger_{\boldsymbol{q}}(\tau)-a_{-\boldsymbol{q}}(\tau)\right),\phi_{-\boldsymbol{q}}(\tau')]\rangle\delta(\tau-\tau')\\ =\;& \omega_{\boldsymbol{q}}^2D(\boldsymbol{q},\tau-\tau')-2\omega_{\boldsymbol{q}}\sum_{\boldsymbol{k}\sigma}M_{\boldsymbol{k}+\boldsymbol{q},\boldsymbol{k}}\langle Tc^\dagger_{\boldsymbol{k}+\boldsymbol{q}\sigma}(\tau)c_{\boldsymbol{k}\sigma}(\tau)\phi_{-\boldsymbol{q}}(\tau')\rangle\\ &+2\omega_{\boldsymbol{q}}\delta(\tau-\tau').\end{aligned} \tag{A.20}$$

[3] We use $\phi_{\boldsymbol{q}}=a^\dagger_{\boldsymbol{q}}+a_{-\boldsymbol{q}}$ because we assume $\phi_{-\boldsymbol{q}}=\phi_{\boldsymbol{q}}$ as mentioned above.

If we approximate the second term of right-hand side to be 0, the equation of motion for the phonon Green's function is as follows.

$$\left[\frac{\partial^2}{\partial\tau^2} - \omega_{\boldsymbol{q}}^2\right] D(\boldsymbol{q}, \tau - \tau') \;\; = \;\; 2\omega_{\boldsymbol{q}}\,\delta(\tau - \tau'). \tag{A.21}$$

From this and (A.17), we get the expression of Γ.

$$\begin{aligned}\Gamma(\boldsymbol{q}, \boldsymbol{k}, \tau, \tau'', \tau') = &- \int_0^\beta d\tau_1 D(\boldsymbol{q}, \tau - \tau_1) \\ &\sum_{\boldsymbol{k}'\sigma} M_{\boldsymbol{k}'+\boldsymbol{q},\boldsymbol{k}'} \langle T c^\dagger_{\boldsymbol{k}'+\boldsymbol{q}\sigma}(\tau_1) c_{\boldsymbol{k}'\sigma}(\tau_1) c_{\boldsymbol{k}+\boldsymbol{q}\uparrow}(\tau'') c^\dagger_{\boldsymbol{k}\uparrow}(\tau')\rangle. \end{aligned} \tag{A.22}$$

If we substitute this into (A.11), we get the equation of motion for the electron Green's function.

$$\begin{aligned}&\left[-\frac{\partial}{\partial\tau} - \xi_{\boldsymbol{k}}\right] G(\boldsymbol{k}, \tau - \tau') \\ &= \delta(\tau - \tau') - \sum_{\boldsymbol{q}} \int_0^\beta d\tau_1 M_{\boldsymbol{k},\boldsymbol{k}+\boldsymbol{q}} D(\boldsymbol{q}, \tau - \tau_1) \\ &\quad \times \sum_{\boldsymbol{k}'\sigma} M_{\boldsymbol{k}'+\boldsymbol{q},\boldsymbol{k}'} \langle T c^\dagger_{\boldsymbol{k}'+\boldsymbol{q}\sigma}(\tau_1) c_{\boldsymbol{k}'\sigma}(\tau_1) c_{\boldsymbol{k}+\boldsymbol{q}\uparrow}(\tau) c^\dagger_{\boldsymbol{k}\uparrow}(\tau')\rangle. \end{aligned} \tag{A.23}$$

If the Mean field approximation is employed,

$$\begin{aligned}&\langle T c^\dagger_{\boldsymbol{k}'+\boldsymbol{q}\sigma}(\tau_1) c_{\boldsymbol{k}'\sigma}(\tau_1) c_{\boldsymbol{k}+\boldsymbol{q}\uparrow}(\tau) c^\dagger_{\boldsymbol{k}\uparrow}(\tau')\rangle \\ \to \;\; &\delta_{\boldsymbol{k}',\boldsymbol{k}}\delta_{\sigma,\uparrow} \langle T c_{\boldsymbol{k}+\boldsymbol{q}\uparrow}(\tau) c^\dagger_{\boldsymbol{k}+\boldsymbol{q}\uparrow}(\tau_1)\rangle \langle T c_{\boldsymbol{k}\uparrow}(\tau_1) c^\dagger_{\boldsymbol{k}\uparrow}(\tau')\rangle \\ - \;\; &\delta_{\boldsymbol{k}',-\boldsymbol{k}-\boldsymbol{q}}\delta_{\sigma,\downarrow} \langle T c_{\boldsymbol{k}+\boldsymbol{q}\uparrow}(\tau) c_{-\boldsymbol{k}-\boldsymbol{q}\downarrow}(\tau_1)\rangle \langle T c^\dagger_{-\boldsymbol{k}\downarrow}(\tau_1) c^\dagger_{\boldsymbol{k}\uparrow}(\tau')\rangle. \end{aligned} \tag{A.24}$$

The anomalous Green's function is defined as follows.

$$F^\dagger(\boldsymbol{k}, \tau - \tau') \;\; \equiv \;\; -\langle T c^\dagger_{-\boldsymbol{k}\downarrow}(\tau) c^\dagger_{\boldsymbol{k}\uparrow}(\tau')\rangle. \tag{A.25}$$

The equation of motion is expressed by using this.

$$\left[-\frac{\partial}{\partial\tau} - \xi_{\boldsymbol{k}}\right] G(\boldsymbol{k}, \tau - \tau')$$

$$
\begin{aligned}
&= \delta(\tau-\tau') - \sum_{\boldsymbol{q}} \int_0^\beta d\tau_1 |M_{\boldsymbol{k}+\boldsymbol{q},\boldsymbol{k}}|^2 D(\boldsymbol{q},\tau-\tau_1) \\
&\quad \times \left[G(\boldsymbol{k}+\boldsymbol{q},\tau-\tau_1) G(\boldsymbol{k},\tau_1-\tau') - F(\boldsymbol{k}+\boldsymbol{q},\tau-\tau_1) F^\dagger(\boldsymbol{k},\tau_1-\tau') \right].
\end{aligned} \tag{A.26}
$$

Let's calculate the Fourier transform of this. The Fourier transform of the Green's function is

$$
G(\boldsymbol{k},\tau-\tau') = \frac{1}{\beta} \sum_n e^{-i\omega_n(\tau-\tau')} G(\boldsymbol{k}, i\omega_n). \tag{A.27}
$$

Here, ω_n is called Matsubara frequency. For integer n, it is defined by

$$
\omega_n \equiv \begin{cases} (2n+1)\pi T & (Fermion), \\ 2n\pi T & (Boson). \end{cases} \tag{A.28}
$$

Therefore,

$$
\begin{aligned}
&\int_0^\beta d\tau_1 D(\boldsymbol{q},\tau-\tau_1) G(\boldsymbol{k}+\boldsymbol{q},\tau-\tau_1) G(\boldsymbol{k},\tau_1-\tau') \\
&= \int_0^\beta d\tau_1 \frac{1}{\beta^3} \sum_{lmn} D(\boldsymbol{q}, i\omega_l) e^{-i\omega_l(\tau-\tau_1)} \\
&\quad \times G(\boldsymbol{k}+\boldsymbol{q}, i\omega_m) e^{-i\omega_m(\tau-\tau_1)} G(\boldsymbol{k}, i\omega_n) e^{-i\omega_n(\tau_1-\tau')} \\
&= \frac{1}{\beta^2} \sum_{lmn} e^{-i(\omega_l+\omega_m)\tau + i\omega_n\tau'} D(\boldsymbol{q}, i\omega_l) \\
&\quad \times G(\boldsymbol{k}+\boldsymbol{q}, i\omega_m) G(\boldsymbol{k}, i\omega_n) \frac{1}{\beta} \int_0^\beta d\tau_1 e^{i(\omega_l+\omega_m-\omega_n)\tau_1} \\
&= \frac{1}{\beta^2} \sum_{mn} e^{-i\omega_n(\tau-\tau')} D(\boldsymbol{q}, i\omega_n - i\omega_m) G(\boldsymbol{k}+\boldsymbol{q}, i\omega_m) G(\boldsymbol{k}, i\omega_n).
\end{aligned} \tag{A.29}
$$

The Fourier transform of $F^\dagger$ is calculated in a similar way.

In addition, from

$$
\left[-\frac{\partial}{\partial\tau} - \xi_{\boldsymbol{k}} \right] G(\boldsymbol{k},\tau-\tau') = (i\omega_n - \xi_{\boldsymbol{k}}) \frac{1}{\beta} \sum_n e^{-i\omega_n(\tau-\tau')} G(\boldsymbol{k}, i\omega_n), \tag{A.30}
$$

$$
\delta(\tau-\tau') = \frac{1}{\beta} \sum_n e^{-i\omega_n(\tau-\tau')}, \tag{A.31}
$$

(A.26) is

$$\begin{aligned}
& (i\omega - \xi_{\boldsymbol{k}})G(\boldsymbol{k}, \tau - \tau') \\
= \; & 1 - T\sum_{\boldsymbol{q}} |M_{\boldsymbol{k}+\boldsymbol{q},\boldsymbol{k}}|^2 \sum_m D(\boldsymbol{q}, i\omega_n - i\omega_m) \\
& \times \left[G(\boldsymbol{k}+\boldsymbol{q}, i\omega_m) G(\boldsymbol{k}, i\omega_n) - F(\boldsymbol{k}+\boldsymbol{q}, i\omega_m) F^\dagger(\boldsymbol{k}, i\omega_n) \right]. \quad \text{(A.32)}
\end{aligned}$$

If we define $\boldsymbol{k}' = \boldsymbol{k} + \boldsymbol{q}$ and assume $D(\boldsymbol{k}' - \boldsymbol{k}) = D(\boldsymbol{k} - \boldsymbol{k}')$,

$$\begin{aligned}
& (i\omega - \xi_{\boldsymbol{k}})G(\boldsymbol{k}, \tau - \tau') \\
= \; & 1 - T\sum_{\boldsymbol{k}'} |M_{\boldsymbol{k}',\boldsymbol{k}}|^2 \sum_m D(\boldsymbol{k}' - \boldsymbol{k}, i\omega_n - i\omega_m) \\
& \times \left[G(\boldsymbol{k}', i\omega_m) G(\boldsymbol{k}, i\omega_n) - F(\boldsymbol{k}', i\omega_m) F^\dagger(\boldsymbol{k}, i\omega_n) \right]. \quad \text{(A.33)}
\end{aligned}$$

The normal self-energy Σ_N and anomalous self-energy Σ_A are defined by

$$\begin{aligned}
\Sigma_N(\boldsymbol{k}, i\omega_n) &\equiv -T\sum_{\boldsymbol{k}'m} |M_{\boldsymbol{k}',\boldsymbol{k}}|^2 D(\boldsymbol{k} - \boldsymbol{k}', i\omega_n - i\omega_m) G(\boldsymbol{k}', i\omega_m), \quad \text{(A.34)} \\
\Sigma_A(\boldsymbol{k}, i\omega_n) &\equiv T\sum_{\boldsymbol{k}'m} |M_{\boldsymbol{k}',\boldsymbol{k}}|^2 D(\boldsymbol{k} - \boldsymbol{k}', i\omega_n - i\omega_m) F(\boldsymbol{k}', i\omega_m). \quad \text{(A.35)}
\end{aligned}$$

Therefore, the equation of motion is as follows.

$$\left[i\omega_n - \xi_{\boldsymbol{k}} - \Sigma_N(\boldsymbol{k}, i\omega_n) \right] G(\boldsymbol{k}, i\omega_n) - \Sigma_A(\boldsymbol{k}, i\omega_n) F^\dagger(\boldsymbol{k}, i\omega_n) = 1. \quad \text{(A.36)}$$

In a similar way, we calculate the equation of motion for anomalous Green's function $F^\dagger$.

$$\left[i\omega_n + \xi_{\boldsymbol{k}} + \Sigma_N(\boldsymbol{k}, -i\omega_n) \right] F^\dagger(\boldsymbol{k}, i\omega_n) - \Sigma_A^*(\boldsymbol{k}, i\omega_n) G(\boldsymbol{k}, i\omega_n) = 0. \quad \text{(A.37)}$$

The (A.34), (A.35), (A.36) and (A.37) are called the Eliashberg equations. Note that the vertex correction is neglected in this formulation. This approximation is guaranteed by the Migdal's theorem.[57]

A.2 Gap equation

In this section, we explain the gap equation to determinate the superconducting gap. T_c can be calculated from the gap equation and the property that the superconducting gap vanishes at $T = T_c$. From this section, $\boldsymbol{k}$ and $i\omega_n$ are omitted except cases that they are important.

Solving the Eliashberg equations (A.36) and (A.37) for $G, F^\dagger$,

$$\begin{pmatrix} G \\ F^\dagger \end{pmatrix} = \frac{1}{[i\omega_n + \xi + \Sigma_N(-i\omega_n)][i\omega_n - \xi - \Sigma_N(i\omega_n)] - |\Sigma_A|^2} \times \begin{pmatrix} i\omega_n + \xi + \Sigma_N(-i\omega_n) \\ \Sigma_A(i\omega_n) \end{pmatrix}. \tag{A.38}$$

Here, Z, χ and Δ are defined as follows.

$$\frac{1}{2}[\Sigma_N(i\omega_n) - \Sigma_N(-i\omega_n)] \equiv i\omega_n[1 - Z(i\omega_n)], \tag{A.39}$$

$$\frac{1}{2}[\Sigma_N(i\omega_n) + \Sigma_N(-i\omega_n)] \equiv \chi(i\omega_n), \tag{A.40}$$

$$\Sigma_A \equiv \Delta Z. \tag{A.41}$$

The Δ is called superconducting gap.

By using these definitions, G and $F^\dagger$ are expressed by

$$\begin{pmatrix} G \\ F^\dagger \end{pmatrix} = \frac{1}{(i\omega_n Z)^2 - (\xi + \chi)^2 - (|\Delta|Z)^2} \begin{pmatrix} \omega_n Z + (\xi + \chi) \\ \Delta Z \end{pmatrix}. \tag{A.42}$$

Because the $i\omega_n$ dependence of χ is small in general, we assume that $\chi(0) = \Sigma(0)$ is included in the quasi-particle band ξ and χ is negligible compared with $i\omega_n$.

From this, (A.34), (A.39) and (A.40), the normal self-energy Σ_N is obtained as follows.

$$\Sigma_N = i\omega_n(1 - Z)$$

$$
\begin{aligned}
&= -T\sum_{\boldsymbol{k}'m} |M_{\boldsymbol{k}\boldsymbol{k}'}|^2 D(\boldsymbol{k}-\boldsymbol{k}', i\omega_n - i\omega_m) G(\boldsymbol{k}', i\omega_m) \\
&= -T\sum_{\boldsymbol{k}'m} \frac{\lambda(\boldsymbol{k},\boldsymbol{k}', n-m)}{N(0)} \frac{\xi + i\omega_m Z}{\xi^2 + Z^2(\omega_m^2 + |\Delta|^2)}. \qquad \text{(A.43)}
\end{aligned}
$$

Here,

$$
\lambda(\boldsymbol{k},\boldsymbol{k}', n-m) \equiv -N(0)|M_{\boldsymbol{k}\boldsymbol{k}'}|^2 D(\boldsymbol{k}-\boldsymbol{k}', i\omega_n - i\omega_m). \qquad \text{(A.44)}
$$

$N(0)$ is the density of states at Fermi level. Note that many textbook define λ using the Eliashberg function $\alpha^2 F(\boldsymbol{k},\boldsymbol{k}',\Omega)$ as follows.

$$
\begin{aligned}
\lambda(\boldsymbol{k},\boldsymbol{k}', n) &\equiv \int_0^\infty d\Omega \alpha^2 F(\boldsymbol{k},\boldsymbol{k}',\Omega) \frac{2\Omega}{\omega_n^2 + \Omega^2}, \qquad \text{(A.45)} \\
\alpha^2 F(\boldsymbol{k},\boldsymbol{k}',\Omega) &\equiv -N(0)|M_{\boldsymbol{k}\boldsymbol{k}'}|^2 \frac{1}{\pi} \mathrm{Im} D(\boldsymbol{k}-\boldsymbol{k}', \Omega + i\eta) \\
&= N(0)|M_{\boldsymbol{k}\boldsymbol{k}'}|^2 \delta(\Omega - \omega_{\boldsymbol{k}-\boldsymbol{k}'}). \qquad \text{(A.46)}
\end{aligned}
$$

Here, the second equation in (A.46) is obtained from assumption that the phonons do not interact with each other.

Approximating the λ to the average at Fermi surface:

$$
\lambda(\boldsymbol{k},\boldsymbol{k}', n) \simeq \lambda(n) \equiv \frac{\sum_{\boldsymbol{k}\boldsymbol{k}'} \lambda(\boldsymbol{k},\boldsymbol{k}', n)\delta(\epsilon_{\boldsymbol{k}})\delta(\epsilon_{\boldsymbol{k}'})}{\sum_{\boldsymbol{k}\boldsymbol{k}'} \delta(\epsilon_{\boldsymbol{k}})\delta(\epsilon_{\boldsymbol{k}'})}, \qquad \text{(A.47)}
$$

and $\sum_{\boldsymbol{k}} \simeq N(0)\int d\xi$, we obtained

$$
\begin{aligned}
i\omega_n(1-Z) &= -T\sum_m \lambda(n-m) \int_{-\infty}^{\infty} d\xi \frac{\xi + i\omega_m Z}{\xi^2 + Z^2(\omega_m^2 + |\Delta|^2)} \\
&= -T\sum_m \lambda(n-m) \frac{i\pi\omega_m}{(\omega_m^2 + |\Delta|^2)^{1/2}}. \qquad \text{(A.48)}
\end{aligned}
$$

When $T \simeq T_c$, the superconducting gap Δ is very small and negligible compared with ω_m.

$$
\omega_n(1-Z) = -\pi T\sum_m \lambda(n-m) \frac{\omega_m}{|\omega_m|}. \qquad \text{(A.49)}
$$

Defining $s_n \equiv \mathrm{sign}(\omega_n) = (2n+1)/|2n+1|$, we solve the equation for Z.

$$
Z(i\omega_n) = 1 + \frac{1}{|2n+1|} \sum_m \lambda(n-m) s_n s_m. \qquad \text{(A.50)}
$$

Calculating for anomalous self-energy Σ_A in a similar way,

$$Z(i\omega_n)\Delta(i\omega_n) = \sum_m \frac{1}{|2m+1|}\lambda(n-m)\Delta(i\omega_m). \tag{A.51}$$

If we eliminate the Z from the two equation, we obtain the gap equation:

$$\Delta(i\omega_n) = \sum_m \frac{1}{|2m+1|}\left[\lambda(n-m) - \delta_{nm}\sum_{m'}\lambda(n-m')s_n s_{m'}\right]\Delta(i\omega_m). \tag{A.52}$$

The superconducting critical temperature T_c is the maximum value of temperature where the equation has a non-trivial solution $\Delta \neq 0$.

A.3 Coulomb interaction

As for the Coulomb interaction V_c, we neglect the vertex correction as same as electron-phonon interaction. Here, you should note that the Migdal's theorem does not hold for the Coulomb interaction.

The self-energy has two type: normal self-energy Σ_N^c and anomalous self-energy Σ_A^c. The contribution of Σ_N^c is already included to the normal Green's function G_N.

We assume that the contribution of normal Green's function G_N to self-energy is already included. The remaining part $\Sigma_N^c = \int V_c(G - G_N)$ is negligible when $T \simeq T_c$. Therefore, we have to deal with only the following equations.

$$\Sigma_A^c(i\omega_n) = -\sum_{\boldsymbol{k}m} V_c(\boldsymbol{k},\boldsymbol{k}')F^\dagger(\boldsymbol{k},i\omega_m) \equiv V_c \circ F^\dagger, \tag{A.53}$$

$$\begin{aligned} V_c(\boldsymbol{k},\boldsymbol{k}') &= \langle \boldsymbol{k}'\uparrow, -\boldsymbol{k}'\downarrow | V_c | \boldsymbol{k}\uparrow, -\boldsymbol{k}\downarrow\rangle \\ &= \int d\boldsymbol{r}\int d\boldsymbol{r}'\int d\boldsymbol{r}''\psi^*_{\boldsymbol{k}'}(\boldsymbol{r})\psi^*_{-\boldsymbol{k}'}(\boldsymbol{r}')\frac{1}{\epsilon(\boldsymbol{r},\boldsymbol{r}'')|\boldsymbol{r}''-\boldsymbol{r}'|}\psi_{\boldsymbol{k}}(\boldsymbol{r})\psi_{-\boldsymbol{k}}(\boldsymbol{r}'). \end{aligned} \tag{A.54}$$

Here, ϵ is the dielectric function.

We divide the range of ω_m into (I) $|\omega_m| < \omega_c$ and (II) $|\omega_m| > \omega_c$, and define V_c^* as the effective interaction convolved with the contribution in (II).

$$\Sigma_A^c = V_c \circ F_{I+II}^\dagger \equiv V_c^* \circ F_I^\dagger. \tag{A.55}$$

In the range (II), the contribution to Σ_A by the phonon is negligible compared with ω. Therefore, using (A.42), we approximate

$$F_{II}^\dagger \simeq \frac{\Sigma_A^c}{\omega_m^2 + \xi^2} \equiv K \circ \Sigma_A^c. \tag{A.56}$$

Then,

$$\Sigma_A^c = V_c \circ F_I^\dagger + V_c \circ F_{II}^\dagger, \tag{A.57}$$

$$\begin{aligned} V_c^* \circ F_I^\dagger &= V_c \circ F_I^\dagger + V_c \circ K \circ \Sigma_A^c \\ &= V_c \circ F_I^\dagger + V_c \circ K \circ V_c^* \circ F_I^\dagger. \end{aligned} \tag{A.58}$$

Therefore, the equation of V_c^* is as follows.

$$V_c^* = V_c + V_c \circ K \circ V_c^*. \tag{A.59}$$

If we neglect the anisotropy and assume that V_c and V_c^* are constants,

$$\begin{aligned} \sum_{\boldsymbol{k}m}^{|\omega_m|>\omega_c} K &= N(0) \sum_m^{|\omega_m|>\omega_c} \int_{-\epsilon_b}^{\epsilon_b} d\xi \frac{1}{\omega_m^2 + \xi^2} \\ &\simeq N(0) \ln\left(\frac{\epsilon_b}{\omega_c}\right). \end{aligned} \tag{A.60}$$

The upper limit of $|\xi|$, $\epsilon_b \gg \omega_c$, is thought to be of the order of band width. We define $\mu \equiv N(0)V_c$ and $\mu^* \equiv N(0)V_c^*$. From (A.55) and (A.59),

$$\Sigma_A^c = T \sum_{\boldsymbol{k}'m}^{|\omega_m|<\omega_c} \frac{\mu^*}{N(0)} F^\dagger(\boldsymbol{k}', i\omega_m), \tag{A.61}$$

$$\mu^* = \frac{\mu}{1 + \mu \ln(\epsilon_b/\omega_c)}. \tag{A.62}$$

Adding this to (A.35) and solving the gap equations, we obtain

$$\Delta(i\omega_n) = \sum_{m}^{|\omega_m|<\omega_c} \frac{1}{|2m+1|}\left[\lambda(n-m) - \mu^* - \delta_{nm}\sum_{m'}\lambda(n-m')s_n s_{m'}\right]\Delta(i\omega_m). \tag{A.63}$$

A.4 McMillan's formula

McMillan's formula is the approximated solution of the gap equation and is used to estimate T_c of phonon-mediated superconductor.

For solving the gap equation, we use the square-well model. For the cut-off frequency $\omega_D = \pi(2N+1)T_c$, this model assumes that in the first term in right-hand side,

$$\lambda(n-m) = \lambda\theta(\omega_D - |\omega_n|)\theta(\omega_D - |\omega_m|), \tag{A.64}$$

and in the third term in right-hand side,

$$\lambda(n-m) = \lambda\theta(\omega_D - |\omega_{n-m}|). \tag{A.65}$$

Here, $\lambda = \lambda(0)$. Therefore,

$$\lambda = 2\int_0^\infty d\Omega \frac{\alpha^2 F(\Omega)}{\Omega}. \tag{A.66}$$

The equation becomes

$$(1+\lambda)\,\Delta(i\omega_n) = (\lambda - \mu^*)\sum_{m}^{|\omega_m|<\omega_D}\frac{\Delta(i\omega_m)}{|2m+1|}. \tag{A.67}$$

If we assume the solution $\Delta(i\omega_n) = \Delta\theta(\omega_D - |\omega_n|)$ and substitute into the equation,

$$\begin{aligned}\frac{1+\lambda}{\lambda-\mu^*} &= \sum_{n=0}^{N-1}\frac{1}{n+1/2} \\ &= \psi\left(\frac{\omega_D}{2\pi T_c}+1\right) - \psi(1/2)\end{aligned}$$

$$\simeq \log\left(\frac{\omega_D}{2\pi T_c}\right) - \log\left(\frac{e^{-\gamma}}{4}\right)$$

$$\simeq \log\left(\frac{1.13\omega_D}{T_c}\right). \tag{A.68}$$

$$T_c = 1.13\omega_D \exp\left(-\frac{1+\lambda}{\lambda-\mu^*}\right). \tag{A.69}$$

Here, $\psi(z)$ is the digamma function and γ is the Euler's constant (See next section).

McMillan calculated this formula and corrected it to agree with the experimental T_c data.[24] After his study, Allen and Dynes made the additional correction and obtained the following formula.[25]

$$T_c = \frac{\omega_{\log}}{1.2} \exp\left(\frac{-1.04(1+\lambda)}{\lambda-\mu^*(1+0.62\lambda)}\right), \tag{A.70}$$

$$\omega_{\log} = \exp\left(\frac{2}{\lambda}\int d\omega \frac{\alpha^2 F(\omega)}{\omega}\log\omega\right). \tag{A.71}$$

This is called McMillan's formula (also called Allen-Dynes formula).

A.5 digamma function

Here, we explain the digamma function and the Euler's constant (also called Euler-Masheroni constant) used at (A.68). The definition of the digamma function $\psi(z)$ is as follows.

$$\psi(z) \equiv \frac{d}{dz}\log\Gamma(z). \tag{A.72}$$

Here, $\Gamma(z)$ is the gamma function.

The following formula is holds due to the property of the gamma function $\Gamma(z+1) = z\Gamma(z)$.

$$\psi(z+1) = \psi(z) + \frac{1}{z}. \tag{A.73}$$

If we change $z \to m + z$ and sum up $m = 1 \sim n$ cases,

$$\psi(n + z + 1) = \psi(z + 1) + \sum_{m=1}^{n} \frac{1}{m + z}. \tag{A.74}$$

For Stirling's formula, if n is large,

$$\begin{aligned} \psi(n + z + 1) &\simeq \psi(n + 1) \\ &= \frac{d}{dn} \log n! \\ &\simeq \frac{d}{dn}(n \log n - n) \\ &= \log n. \end{aligned} \tag{A.75}$$

The definition of the Euler's constant is

$$\gamma \equiv \lim_{n \to \infty} \left(\sum_{m=1}^{n} \frac{1}{m} - \log n \right). \tag{A.76}$$

Therefore, at the limit for $n \to \infty$, (A.74) becomes

$$\psi(z + 1) = -\gamma - \sum_{m=1}^{\infty} \left(\frac{1}{m + z} - \frac{1}{m} \right). \tag{A.77}$$

If $z = -1/2$,

$$\begin{aligned} \psi(1/2) &= -\gamma - 2 \sum_{m=1}^{\infty} \left(\frac{1}{2m - 1} - \frac{1}{2m} \right) \\ &= -\gamma - 2 \left(1 - \frac{1}{2} + \frac{1}{3} - \frac{1}{4} \cdot \cdot \right) \\ &= -\gamma - 2 \log 2 \\ &= \log \left(\frac{e^{-\gamma}}{4} \right). \end{aligned} \tag{A.78}$$

Therefore, (A.68) holds.

Bibliography

[1] M. Affronte, O. Laborde, G. L. Oleese and A. Palenzona: J. ALloys Compd. **274** (1998) 68.

[2] P. Bordet, M. Affronte, S. Sanfilippo, M. Nunez-Regueiro, O. Laborde, G. L. Olcese, A. Palenzona, S. LeFloch, D. Levi and M. Hanfland: Phys. Rev. B **62** (2000) 11392.

[3] S. Sanfilippo, H. Elsinger, M. Nunez-Regueiro, O. Laborde, S. LeFloch, M. Affronte, G. L. Olcese and A. Palenzona: Phys. Rev. B **61** (2000) R3800.

[4] K. Kusakabe, T. Ogitsu and S. Tsuneyuki: J. Phys.: Condens. Matter **10** (1998) 11561.

[5] J. Nagamatsu, N. Nakagawa, T. Muranaka, Y. Zenitani and J. Akimitsu: Nature **410** (2001) 63.

[6] J.H. Weaver, A. Franciosi and V.L. Moruzzi: Phys. Rev. B **29** (1984) 3293.

[7] S. Fahy and D.R. Hamann: Phys. Rev. B **41** (1990) 7587.

[8] G. Satta, G. Profeta, F. Bernardini, A. Continenza and S. Massidda: Phys. Rev. B **64** (2001) 104507.

[9] J.L. Wang, Z. Zeng and Q.Q. Zheng: Physica C **408-410** (2004) 264.

[10] P. Hohenberg and W. Kohn : Phys. Rev. **136** (1964) B864.

[11] W. Kohn and L. J. Sham : Phys. Rev. **140** (1965) A1133.

[12] P. Giannozzi, S. Baroni, N. Bonini, M. Calandra, R. Car, C. Cavazzoni, D. Ceresoli, G. L. Chiarotti, M. Cococcioni, I. Dabo, A. Dal Corso, S. Fabris, G. Fratesi, S. de Gironcoli, R. Gebauer, U. Gerstmann, C. Gougoussis, A. Kokalj, M. Lazzeri, L. Martin-Samos, N. Marzari, F. Mauri, R. Mazzarello, S. Paolini, A. Pasquarello, L. Paulatto, C. Sbraccia, S. Scandolo, G. Sclauzero, A. P. Seitsonen, A. Smogunov, P. Umari, R. M. Wentzcovitch: J. Phys.: Condens. Matter, **21** (2009) 395502

[13] J. P. Perdew, J. A. Chevary, S. H. Vosko, K. A. Jackson, M. R. Pederson, D. J. Singh, and C. Fiolhais : Phys. Rev. B **46** (1992) 6671.

[14] David Vanderbilt : Phys. Rev. B **41** (1990) 7892.

[15] M. Parrinello and A. Rahman : Phys. Rev. Lett. **45** (1980) 1196.

[16] H. J. Monkhorst and J. D. Pack : Phys. Rev. B **13** (1976) 5188.

[17] G.M. Eliashberg: Zh. Eksp. Teor. Fiz. **38** (1960) 966; Sov. Phys. JETP **11** (1960) 696.

[18] S. Baroni, S. de Gironcoli, A. Dal Corso, and P. Giannozzi : Rev. Mod. Phys. **73** (2001) 515.

[19] S. Y. Savrasov and D. Y. Savrasov: Phys. Rev. B **54** (1996) 16487, and the references therein.

[20] P. Blaha, K. Schwarz, G. K. H. Madsen, D. Kvasnicka and J. Luitz: WIEN2k, An Augmented Plane Wave + Local Orbitals Program for

Calculating Crystal Properties (Karlheinz Schwarz, Tech. Universities Wien, Austria, 2001) ISBN 3-9501031-1-2.

[21] T. Ishikawa, A. Ichikawa, H. Nagara, M. Geshi, K. Kusakabe and N. Suzuki: Phys. Rev. B **77** (2008) 020101.

[22] J. Kortus, I. I .Mazin, K. D. Belashchenko, V. P. Antropov and L. L. Boyer: Phys. Rev. Lett. **86** (2001) 4656.

[23] For a test calculation, we estimated T_c of MgB_2 in the present scheme. The estimation tells $T_c \simeq 25$K. This is close to the known value obtained with approximations same as the present study.

[24] W. L. McMillan: Phys. Rev. **167** (1968) 331.

[25] P. B. Allen and R. C. Dynes: Phys. Rev. B **12** (1975) 905.

[26] K.-P. Bohnen, R. Heid and B. Renker: Phys. Rev. Lett. **86** (2001) 5771.

[27] S.U. Maheswari, H. Nagara, K. Kusakabe and N. Suzuki: J. Phys. Soc. Jpn. **74** (2005) 3227.

[28] M. Karuzawa, M. Ishizuka, and S. Endo: J. Phys.: Condens. Matter **14** (2002) 10759.

[29] Y. Akahama, M. Kobayashi and H. Kawamura: Phys. Rev. B **59** (1999) 8520.

[30] I. Hamada, T. Oda and N. Suzuki: *Science and Technology of High Pressure, Proceeding of AIRAPT-17* (University Press, Delhi, India, 2000), vol. 1, p. 467.

[31] Y. Akahama and H. kawamura: Phys. Rev. B **61** (2000) 3139.

[32] R. Ahuja: Phys. Status Solidi B **235** (2003) 282.

[33] F. J. H. Ehlers and N. E. Christensen: Phys. Rev. B **69** (2004) 214112.

[34] T. Ishikawa, H. Nagara, K. Kusakabe, and N. Suzuki: Phys. Rev. Lett. **96** (2006) 095502.

[35] H. Fujihisa, Y. Akahama, H. Kawamura, Y. Ohishi, Y. Gotoh, H. Yamawaki, M. Sakashita, S. Takeya, and K. Honda: Phys. Rev. Lett. **98** (2007) 175501.

[36] J.P.Perdew, K.Burke, M.Ernzerhof, Phys. Rev. Lett. **77**, 3865 (1996)

[37] T. Ishikawa: Dr. Thesis, Faculty of Science, Osaka University, Osaka, 2008.

[38] M. Marqués, G. J. Ackland, L. F. Lundegaard, S. Falconi, C. Hejny, M. I. McMahon, J. Contreras-García, and M. Hanfland : Phys. Rev. B **78** (2008) 054120.

[39] Y. Kamihara, H. Hiramatsu, M. Hirano, R. Kawamura, H. Yanagi, T. Kamiya and H. Hosono: J. Am. Chem. Soc. **128** (2006) 10012.

[40] Y. Kamihara, T. Watanabe, M. Hirano and H. Hosono: J. Am. Chem. Soc. **130** (2008) 3296.

[41] H. Takahashi, K. Igawa, K. Arii, Y. Kamihara, M. Hirano and H. Hosono: Nature **453** (2008) 376.

[42] D. R. Parker, M. J. Pitcher, P. J. Baker, I. Franke, T. Lancaster, S. J. Clarke: Chem. Commun. (2009) 2189.

[43] C. W. Chu, F. Chen, M. Gooch, A. M. Guloy, B. Lorenz, B. Lv, K. Sasmal, Z. H. Tand, J. H. Tapp and Y. Y. Xue: Physica C **469** (2009) 326.

[44] R. A. Jishi and H. M. Alyahyaei: Adv. in Condens. Matter. Phys. **2010** (2010) 6.

[45] D. J. Singh: Phys. Rev. B **78** (2008) 094511.

[46] H. Katayama-Yoshida, T. Koyanagi, H. Funashima, H. Harima, A. Yanase: Solid State Communication **126** (2003) 135.

[47] Chalcopyrite structure belongs to the space group I$\bar{4}$2d (No.122).
Cell vectors are: $\mathbf{a_1} = a(1,0,0), \mathbf{a_2} = a(0,1,0), \mathbf{a_3} = a(0,0,c/a)$.
Wyckoff positions:
Cu(4a)$(0,0,0),(1/2,1/2,1/2),(1/2,0,3/4),(0,1/2,1/4)$,
Al(4b)$(0,0,1/2),(1/2,1/2,0),(1/2,0,1/4),(0,1/2,3/4)$,
O (8d)$(x,1/4,1/8),(-x,-1/4,1/8),(1/4,-x,-1/8),(-1/4,x,-1/8)$
$(x+1/2,3/4,5/8),(-x+1/2,1/4,5/8),(3/4,-x+1/2,3/8),(1/4,x+1/2,3/8)$.

[48] R. W. G. Wyckoff: *Crystal Structures* (Wiely, New York, 1964) 2nd ed., Vol. 2, p.292.

[49] The delafossite structure belongs to the space group R$\bar{3}$m (No.166).
The unit cell is represented by a hexagonal cell or a rhombohedral cell.
a) hexagonal cell
Cell vectors are:
$\mathbf{a_{h1}} = a_h(1,0,0), \mathbf{a_{h2}} = a_h(-1/2,\sqrt{3}/2,0), \mathbf{a_{h3}} = a_h(0,0,c_h/a_h)$.
Wyckoff positions:
Cu(3a)$(\,0,\,0,\,0),(\,2/3,\,1/3,\,1/3),(\,1/3,\,2/3,\,2/3)$,

Al(3b)(0, 0, 1/2), (2/3, 1/3, 5/6), (1/3, 2/3, 1/6),
O (6c)(0, 0, z), (2/3, 1/3, $z + 1/3$), (1/3, 2/3, $z + 2/3$),
(0, 0, $-z$), (2/3, 1/3, $-z + 1/3$), (1/3, 2/3, $-z + 2/3$).

b) rhombohedral cell
Cell vectors are:
$\mathbf{a_{r1}} = a_r(1, 0, c_r/(\sqrt{3}a_r))$, $\mathbf{a_{r2}} = a_r(-1/2, \sqrt{3}/2, c_r/(\sqrt{3}a_r))$,
$\mathbf{a_{r3}} = a_r(-1/2, -\sqrt{3}/2, c_r/(\sqrt{3}a_r))$.
Here, $a_r = a_h/\sqrt{3}, c_r = c_h/\sqrt{3}$.
Wyckoff positions:
Cu(1a) $(0, 0, 0)$, Al(1b) $(1/2, 1/2, 1/2)$, O(2c) $\pm(z, z, z)$.

[50] N. E. Christensen, A. Svane, R. Laskowski, B. Palanivel, P. Modak, A. N. Chantis, M. van Schilfgaarde, and T. Kotani: Phys. Rev. B **81** (2010) 045203.

[51] P. Rodríguez-Hernández, A. Muñoz, J. Pellicer-Porres, D. Martínez-García, A. Segura, N. Garro, J. C. Chrvin, and D. Kim: Phys. Stat. Sol. (b) **244**, No.1, (2007) 342.

[52] S. Gilliland, J. Pellicer-Porres, A. Segura, A. Muñoz, R. Rodríguez-Hernández, D. Kim, M. S. Lee, and T. Y. Kim: Phys. Stat. Sol. (b) **244**, No.1, (2007) 309.

[53] A. Filippetti and N. A. Spaldin: Phys. Rev. B **67** (2003) 125109.

[54] D. Vogel, P.Krüger and J. Pollmann: Phys. Rev. B **54** (1996) 5495.

[55] J. P. Perdew and A. Zunger: Phys. Rev. B **23** (1981) 5048.

[56] *Semiconductors Physics of Group IV elements and III-V Compounds*, edited by K. H. Hellwge and O. Madelung, Landolt-Börnstein, New Series, Group III Vol. 17 (Springer, Berlin, 1982); *Intrinsic Properties of Group IV elements and III-V,II-VI, and I-VII Compounds*, edited by K. H. Hellwge and O. Madelung, Landolt-Börnstein, New Series, Group III Vol. 22 (Springer, Berlin, 1987).

[57] A. B. Migdal, Zh. Eksp. Teor. Fiz. **34**, 1438 (1958); Sov. Phys. JETP **7**, 996 (1958).

Publication list

1. "Theoretical Evidences for Enhanced Superconducting Transition Temperature of $CaSi_2$ in a High-Pressure AlB_2 Phase", A. Nakanishi, T. Ishikawa, H. Nagara and K. Kusakabe: J. Phys. Soc. Jpn. **77** (2008) 104712.

2. "Origin of Enhanced Superconducting Transition Temperature Through Structural Transformation in $CaSi_2$", A. Nakanishi, T. Ishikawa, H. Nagara and K. Kusakabe: J. Phys.:Conf. Ser. **121** (2008) 052010.

3. "General Rule and Materials Design of Negative Effective U System for High-T_c Superconductivity", H. Katayama-Yoshida, H. Kusakabe, H. Kizaki, A. Nakanishi: Appl. Phys. Express **1** (2008) 081703.

4. "First-Principles Study of NaFeAs, NaCoAs, and NaNiAs", K. Kusakabe and A. Nakanishi: J. Phys. Soc. Jpn. **78** (2009) 124712.

5. "Pressure-induced structural transition and enhancement of energy gap of $CuAlO_2$", A. Nakanishi and H. Katayama-Yoshida: J. Phys. Soc. Jpn. **80** (2011) 024706.

6. "Computational Material Design for High Critical Temperature Superconductivity in Hole-Doped $CuAlO_2$: Transparent Superconductors", A. Nakanishi and H. Katayama-Yoshida: submitted to Appl. Phys. Express.